NATIONAL TECHNICAL UNIVERSITY OF ATHENS
SCHOOL OF NAVAL ARCHITECTURE &
MARINE ENGINEERING

DIPLOMA THESIS

Optimal heat transfer enhancement in flow past a partially hydrophobic circular cylinder

SPYRIDON T. KAFARAKIS

Thesis Committee:

Supervisor: L. Kaiktsis, Associate Professor N.T.U.A.
Members: G.S. Triantafyllou Professor N.T.U.A.
               C.I. Papadopoulos, Assistant Professor N.T.U.A.

Athens, October 2015

ΕΘΝΙΚΟ ΜΕΤΣΟΒΙΟ ΠΟΛΥΤΕΧΝΕΙΟ
ΣΧΟΛΗ ΝΑΥΠΗΓΩΝ ΜΗΧΑΝΟΛΟΓΩΝ
ΜΗΧΑΝΙΚΩΝ

ΔΙΠΛΩΜΑΤΙΚΗ ΕΡΓΑΣΙΑ

Βέλτιστη ενίσχυση μεταφοράς θερμότητας σε ροή γύρω από μερικώς υδροφοβικό κύλινδρο

 ΣΠΥΡΙΔΩΝ Θ. ΚΑΦΑΡΑΚΗΣ

Εξεταστική Επιτροπή:

Επιβλέπων: Λ. Καϊκτσής, Αναπληρωτής Καθηγητής Ε.Μ.Π.
Members: Γ.Σ. Τριανταφύλλου, Καθηγητής Ε.Μ.Π.
          Χ.Ι. Παπαδόπουλος, Επίκουρος Καθηγητής Ε.Μ.Π.

Αθήνα, Οκτώβριος 2015

ACKNOWLEDGEMENTS

ABSTRACT

Flows past bluff bodies are the subject of various studies due to their extensive applications in constructions and several other applications of engineering. Typical examples of constructions behaving as bluff bodies are skyscrapers and wind generator pylons (ashore applications), and oil risers (offshore applications). Another important engineering application is the heat exchanger. Main considerations in these application concern the reduction or even cancellation of time dependent forces (which may lead to structural failure due to fatigue), the heat transfer enhancement, as well as the minimization of construction and operation costs. A main challenge in a number of these application is thus the simultaneous reduction of forces on the body and the enhancement of heat transfer.

The scope of the present thesis is the computational study of forced convection heat transfer in flow past a hydrophobic cylinder, at constant surface temperature. Hydrophobic surfaces are applied in flow control applications, since they enable flow slip past a solid boundary; as a result, they can contribute to flow stabilization. At the same time, hydrophobic surfaces are a potential means for heat transfer enhancement.

In the present study, the effects of implementing surface hydrophobicity on the cylinder are investigated, in particular the effects on flow stability and on enhancing heat transfer from the cylinder surface. Here, we consider the low Reynolds number range in which the flow remains two-dimensional, at a constant value of Prandtl number value, equal to unity. The Navier model is utilized for modeling the fluid slip at the solid boundary.

In a first step, slip conditions are applied on the entire cylinder surface. The results demonstrate an increasing trend in both flow stabilization and heat transfer enhancement, at increasing non-dimensional slip length. However, it is noticed that, in the region around the rear stagnation point, application of hydrophobicity does support flow stabilization, and decreases the local heat transfer rate. Thus, application on only a part of the cylinder is considered, (partial slip), with the aim of supporting flow stabilization and heat transfer enhancement, at a reduced control effort.

To this end, a multi-objective optimization problem is formulated and solved aiming at simultaneously: (a) enhancing heat transfer, (b) stabilizing the flow, and (c) reducing the control effort associated with implementing surface hydrophobicity. The optimization results demonstrate that an optimal implementation of partial slip can simultaneously lead to flow stabilization and a substantial heat transfer enhancement, by utilizing significantly lower levels of control effort, in comparison to full slip.

ΣΥΝΟΨΗ

Οι ροές γύρω από μη αεροδυναμικά σώματα αποτελούν αντικείμενο μελέτης εξαιτίας της ευρύτητας των εφαρμογών που έχουν στον κατασκευαστικό και μηχανολογικό τομέα. Τυπικά παραδείγματα κατασκευών που συμπεριφέρονται ως μη αεροδυναμικά σώματα στην ξηρά είναι τα ψηλά κτήρια και οι πυλώνες ανεμογεννητριών, στη θάλασσα οι αγωγοί μεταφοράς υδρογονανθράκων, και σε μηχανολογικές κατασκευές οι εναλλάκτες θερμότητας. Στόχος σε αυτές τις κατασκευές είναι τόσο η αποφυγή των εναλλασσόμενων φορτίσεων όσο και η βελτίωση της μεταφοράς θερμότητας.

Αντικείμενο της παρούσας εργασίας είναι η υπολογιστική εξέταση των χαρακτηριστικών της εξαναγκασμένης μεταφοράς θερμότητας με συναγωγή σε ροή γύρω από υδροφοβικό κύλινδρο υπό σταθερή θερμοκρασία. Οι υδροφοβικές επιφάνειες βρίσκουν εφαρμογή σε προβλήματα ροϊκού ελέγχου, καθώς επιτρέπουν την ολίσθηση της ροής κατά μήκος ενός στερεού ορίου. Με αυτόν τον τρόπο, μπορούν να οδηγήσουν σε σταθεροποίηση της ροής. Ταυτόχρονα, αποτελούν μια υποψήφια μέθοδο για την ενίσχυση της μεταφοράς θερμότητας.

Στην παρούσα εργασία εξετάζονται τόσο οι σταθεροποιητικές και αποσταθεροποιητικές επιδράσεις της υδροφοβικότητας, όσο και η συμβολή της στην αύξηση της μεταφοράς θερμότητας, για χαμηλές τιμές αριθμού Reynolds και για τιμή του αριθμού Prandtl ίση με τη μονάδα. Η υδροφοβικότητα μοντελοποιείται με τη χρήση του μοντέλου Navier.

Αρχικά, όταν η υδροφοβικότητα εφαρμόζεται σε όλη την επιφάνεια του κυλίνδρου, η αύξηση του μήκους ολίσθησης του υδροφοβικού υλικού οδηγεί σε σταθεροποίηση της ροής και σε αύξηση της μεταφοράς θερμότητας από τον κύλινδρο στο ρευστό. Εντούτοις, γίνεται φανερό ότι στην περιοχή του πίσω σημείου ανακοπής η εφαρμογή υδροφοβικότητας συντελεί τόσο στην αποσταθεροποίηση της ροής όσο και στη μείωση της μεταφοράς θερμότητας. Για αυτόν τον λόγο εξετάζεται η εφαρμογή υδροφοβικότητας σε τμήμα της επιφάνειας του κυλίνδρου, γεγονός το οποίο συντελεί και στη μείωση του σχετικού κατασκευαστικού κόστους.

Οι παραπάνω στόχοι οδηγούν στη διαμόρφωση και επίλυση ενός πολύ-κριτηριακού προβλήματος βελτιστοποίησης με στόχους (α) την ενίσχυση της μεταφοράς θερμότητας, (β) την αναίρεση της αστάθειας της ροής, και (γ) τη μείωση του κόστους κατασκευής και της έκτασης της υδροφοβικής επιφάνειας. Τα αποτελέσματα της βελτιστοποίησης καταδεικνύουν ότι η κατάλληλη εφαρμογή υδροφοβικότητας σε τμήμα της επιφάνειας του κυλίνδρου μπορεί να οδηγήσει τόσο σε σημαντική ενίσχυση της μεταφοράς θερμότητας, όσο και σε σταθεροποίηση της ροής, χρησιμοποιώντας σημαντικά χαμηλότερα επίπεδα δράσης ελέγχου.

TABLE OF CONTENTS

LIST OF FIGURES

LIST OF TABLES

1. INTRODUCTION

1.1 Flows past bluff bodies

A large number applications in the field of fluid mechanics concern flows past bluff bodies. The term 'bluff body' refers to an object placed perpendicular to a flow and whose length, measured in the direction of flow, is similar to the width, measured in the direction vertical to the flow. Wind moving past skyscrapers, flow over a moving truck and sea water moving past oil risers, are some examples of bluff-body flows. In the field of engineering a representative bluff body application, concerning also heat transfer, is the heat exchanger. Because of the shape of these bodies, there exists a region of considerable size behind them, termed as 'the wake', where the flow is slowed down. In bluff body flows the wake is characterized by the presence of a double row of alternate concentrated vortices, known as the Kármán vortex street. The latter is the source of oscillating cross-flow forces that may induce significant oscillations of a structure which may lead to structural failure.

The most common bluff body prototype is the circular cylinder with other examples being the square (Fig.1a) and the triangle and the trapezoid cylinder. In comparison with aerodynamic bodies, as the airfoil (Fig. 1b), bluff bodies have drag coefficients that are at least one order of magnitude larger, due to the remarkable increase in pressure drag deriving from the boundary layer separation.

(a)	(b)
(c)	(d)
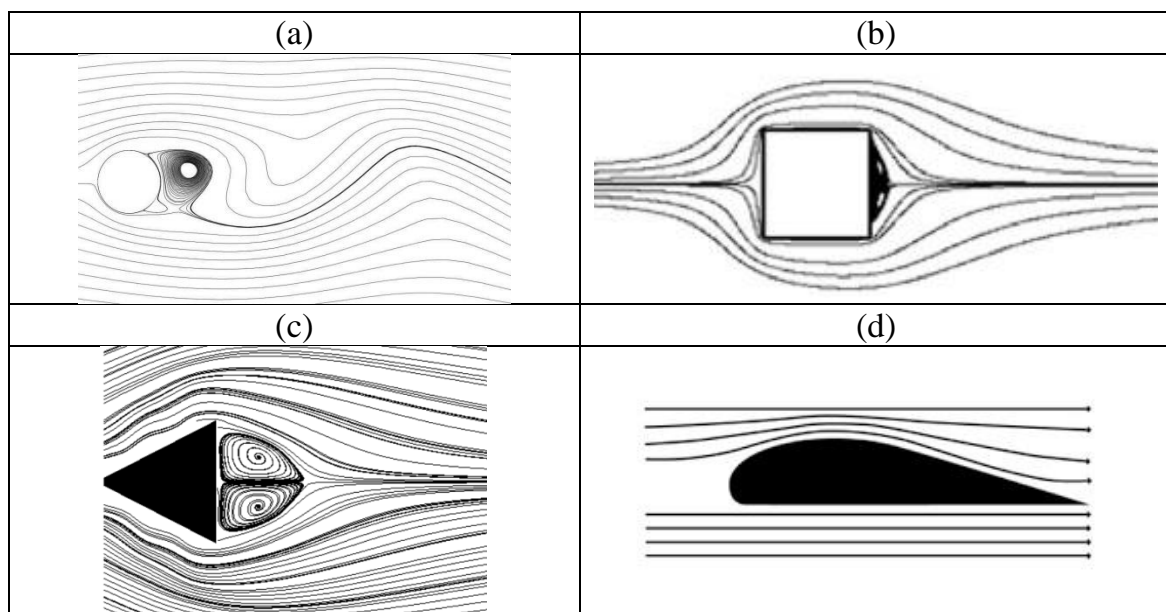
Fig. 1. Bluff body prototypes: (a) circular cylinder, (b) square cylinder, (c) triangular cylinder and aerodynamic body prototype: (d) airfoil.

1.2 Flow past a circular cylinder

A representative bluff body flow, being subject of several experimental and computational investigations, is the flow past a circular cylinder. The major non-dimensional quantity describing the flow physics is the Reynolds number, *Re*, defined in general as the ratio of momentum forces to viscous forces. In a flow past a circular cylinder, the Reynolds number is given in the following form:

$$Re = \frac{D \cdot U}{\nu} \tag{1}$$

where *D* is the diameter of the cylinder, *U* is the velocity of the flow and *v* is the kinematic viscosity of the fluid. It should be noted, that the flow dynamics around a stationary circular cylinder depends only on the Reynolds number, due to the lack of external forces.

1.2.1 Flow Structure

As the Reynolds number increases, the flow structure is modified in the wake region and in the boundary layer of the cylinder. Fig.2 presents the flow structure as a function of the Reynolds number.

For low Reynolds number values (*Re*<180) the flow is two-dimensional and the following cases are distinguished. In more detail, for *Re*<5, the flow follows the geometry of the cylinder to the rear stagnation point, where it is detached (creeping flow). Further, for 5<*Re*<47 the flow continues to be stable, however it is detached earlier than the rear stagnation point forming a symmetrical pair of vortices. The length of this pair of vortices, commonly referred to as the recirculation zone, is increased linearly with increasing Reynolds number, *Re*. Finally, for *Re*>47 the flow develops an unsteady flow known as the Kármán vortex street. At this point, the previously fixed vortices begin to oscillate leading to the detachment of one of them from the wake of the cylinder. The second vortex is shed while the first one is shaped again. This phenomenon is called as the vortex shedding. The vortices appear and are shed alternatively at a specific frequency, *f*. The latter is described by the non-dimensional Strouhal number, *St* (defined in Equation 2). The described particularity of the flow regime (*Re*>47) is known as the Strouhal instability.

$$St = \frac{f \cdot D}{U} \tag{2}$$

For Reynolds number values $Re>180$ the flow becomes three-dimensional and turbulence appear in the wake region of the cylinder. The transitional regime from laminar wake flow to turbulent wake flow is observed at $180<Re<300$, as for $Re>300$ the wake is fully turbulent. Further,in the Reynolds number regime, $300<Re<3{\cdot}10^5$, the flow remains turbulent at the wake region of the cylinder but still laminar at the boundary layers and is known as the sub-critical flow regime. At this point, by increasing Reynolds number even more, $Re>3{\cdot}10^5$, the boundary layers become turbulent at the separation point, however this occurs exclusively at one side of the cylinder, while the other one remains laminar, until $Re=3.5{\cdot}10^5$. Further increase of the Reynolds number, $Re>3.5{\cdot}10^5$, results in both boundary layers separation becoming turbulent. However, the flow is not fully turbulent on neither side of the cylinder until $Re=1.5{\cdot}10^6$, when one of the boundary layers becomes fully turbulent. Finally, at $Re>4.5{\cdot}10^6$ the flow is turbulent everywhere.

$0 < Re < 5$

$5 < Re < 47$

$47 < Re < 180$

$180 < Re < 300$

$300 < Re$

$Re < 3 \cdot 10^5$

$3.5 \cdot 10^5 < Re$

$4.5 \cdot 10^6 < Re$
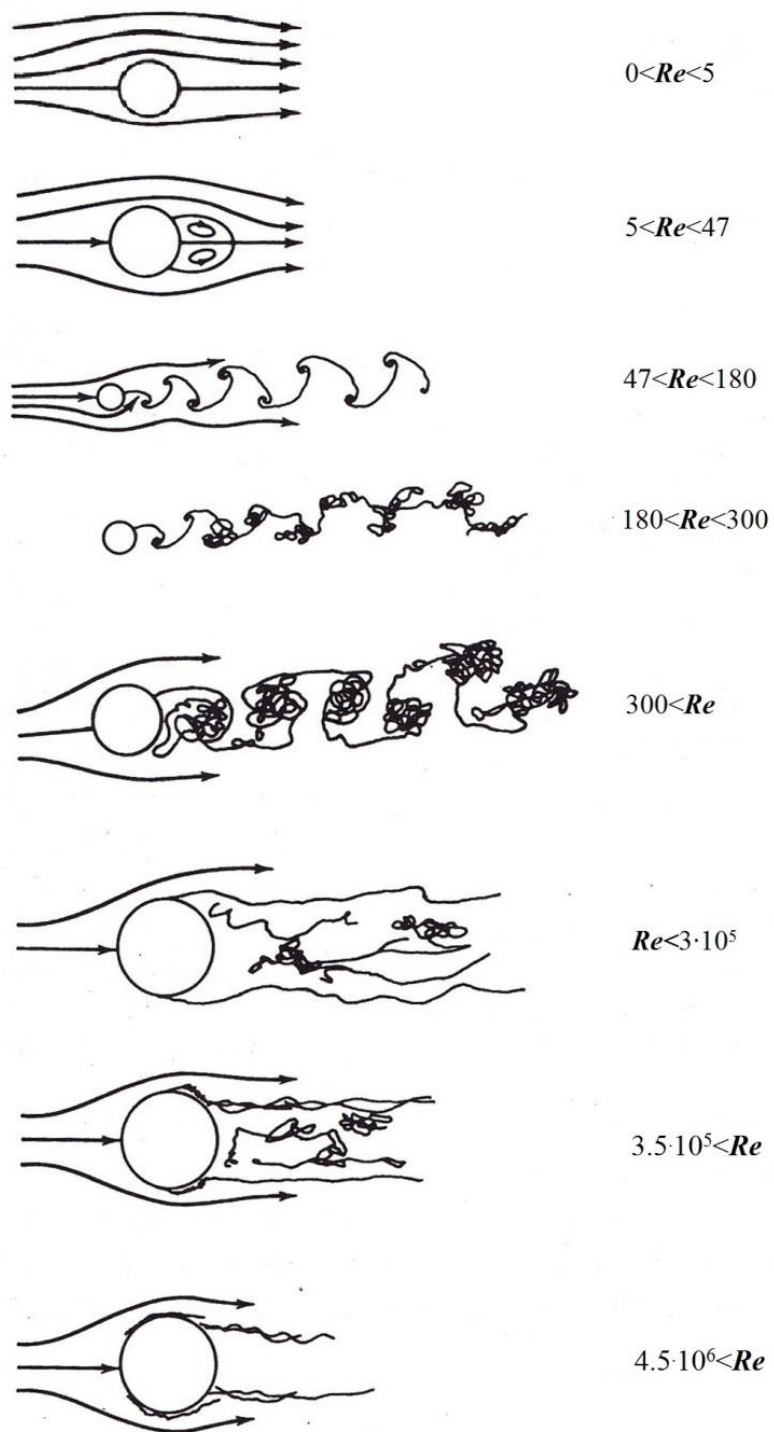
Fig. 2. Flow past a circular cylinder: wake structure for various Reynolds number regimes.

1.2.2 Drag and Lift Forces

The formation of the Kármán vortex street results in the application of an oscillating force on the cylinder. The stream-wise and vertical components of this force are defined as the drag force, F_D, and the lift force, F_L, respectively. The amplitude of the Lift force is much greater than that of the drag force; however, the latter has a double frequency in comparison with the lift force. This occurs because the total period of the drag force is influenced by every vortex that is shed, while the lift force by a pair of vortices. The non-dimensional form of the drag and lift forces are defined as the drag and lift force coefficients, as follows:

$$\text{Drag coefficient: } C_D = \frac{F_D}{\frac{1}{2} \cdot \rho \cdot U^2 \cdot A} \tag{3}$$

$$\text{Lift coefficient: } C_L = \frac{F_L}{\frac{1}{2} \cdot \rho \cdot U^2 \cdot A} \tag{4}$$

where, ρ is the density of the fluid, U the velocity of the flow and A the reference area defined as $A = D \cdot z$, with z being the cylinder's height.

1.3 Heat transfer

1.3.1 Heat transfer mechanism

Heat transfer is the transfer of energy as heat due to temperature differences. Heat transmission is engaged in the study of the mechanisms through which bodies can exchange energy, which are not in equilibrium state in contrast to the thermodynamic and uses fluid dynamics to problems where there is a fluid in motion. Heat, as is well known, is transmitted from higher to lower levels of heat. The transmission mechanisms are the following: (a) conduction, (b) convection and (c) radiation.

The heat transfer mechanism of conduction in fluids is due to the irregular motion (collision) of its particles. The transmission of this energy through random collisions of molecules is called diffusion. As the temperature increases the irregular motion of the particles increases and thus the conduction rate increases (this is more noticeable for gases as for liquids there is the influence of the molecular forces). Moreover, in the case of stationary liquid, interactions between molecules are much stronger due to the presence of strong intermolecular forces. The latter results in an increase of the dissipation of energy through the interaction between molecules. The heat transfer due to conduction is described by Fourier's

Law. Fourier's Law is determines the heat flow as a function of the temperature distribution in the medium. The general form for multidimensional conduction is given by:

$$\vec{q}'' = -k\vec{\nabla}T \tag{5}$$

where $\vec{q}''$ is the local heat flux density, k is the thermal conductivity and $\vec{\nabla}T$ is the temperature gradient. The negative sign in equation (5) is due to the fact that heat always flows towards the lower temperature, which is opposite to the direction set by the differential temperature gradient. Moreover, the thermal conductivity, k, is a measure of how well a material conducts heat and can be defined by equation (5). In general the thermal conductivity depends on the material and correlates with a temperature.

The heat transfer mechanism inside a moving fluid is called convection. The heat transfer by convection is generally complex because it includes heat transfer due to the motion of the fluid and due to heat conduction on the boundary layer between a solid body and the particular liquid. Further, at the case of heat transfer through a fluid, the contribution to the heat transfer rate is much higher by convection compared with that by conduction, as it is proportional to the fluid's velocity. In general, conduction is distinguished as natural or forced regarding the cause of the fluid's movement. In natural convection the movement of fluid is due to natural causes such as gravity or buoyancy, while in forced convection it is due to external forces. The convection depends mainly on the properties of the fluid such as the thermal conductivity, k, the density, ρ, the dynamic viscosity, μ, the specific heat capacity, C_P and the velocity, u. Also, the roughness and shape of the surface, and the type of fluid flow are factors which affect the heat transfer by convection. The general equation describing the heat transfer by convection is Newton's law of cooling:

$$\vec{q}'' = h\left(T_w - T_{inf}\right) \tag{6}$$

where h is the local convective heat transfer coefficient, T_w is the temperature of the solid boundary surface and T_{inf} the temperature of the undisturbed flow, away from the solid body.

When there is a temperature difference between a fluid and a solid body, the thermal boundary layer is formed, in correspondence with the hydrodynamic boundary layer; the latter is created when a moving fluid encounters a solid body. The particles of the fluid in contact with the plate come to thermal equilibrium with it and exchange energy with their adjacent ones. Thus, the temperature transitions smoothly from the

temperature of the wall, T_w, to the temperature away from the wall, T_{inf}. The thickness of the boundary layer is defined as:

$$\delta_t \to \frac{T_w - T(n)}{T_w - T_{inf}} = 0.99 \qquad (7)$$

where $T(n)$ is the temperature of a point at a distance, n, normal to the solid body surface.

Practically, Equation (7) states that the boundary layer thickness is the distance where the fluid has almost attained the temperature of the fluid away from the solid body. Furthermore, when the fluid velocity at the boundary surface is zero (non-slip condition), the heat transfer from the solid body to the fluid is transmitted only by diffusion. In the opposite case, when the fluid is moving on the boundary surface (slip condition) the heat transfer is transmitted by diffusion, but primarily by convection. In general, heat transfer depends on both the thermal and the hydrodynamic boundary layer thicknesses. The non-dimensional quantities describing the heat transfer between a solid body and a fluid depend on the Prandtl number, Pr, defined as:

$$Pr = \frac{\mu C_P}{k} \qquad (8)$$

The Prandtl number quantifies the relative effectiveness of the momentum and the energy by diffusion in the boundary layer velocity and thermal boundary layer respectively and depends only on the type and condition of the fluid under study. Specifically, the Prandtl number of the gases is close to unity, which implies that the transmission of momentum and transmission of energy by diffusion are comparable. Thus, in this case the thickness of the momentum boundary layer is equal to the thickness of the thermal boundary layer.

In a heat exchange problem, the non-dimensional quantity describing the efficiency of convection in comparison with conduction, is the Nusselt number, Nu, defined as:

$$Nu = \frac{h L_c}{k} \qquad (8)$$

where L_c is the characteristic length of the corresponding problem in study.

In particular, in the flow past a circular cylinder, the characteristic length, L_c equals the diameter of the cylinder, D, and thus Equation (8) becomes:

$$Nu = \frac{hD}{k} \qquad (9)$$

The Nusselt number quantifies the heat transfer enhancement due to a fluids motion through the mechanism of convection.

1.3.2 Heat transfer in wake flows

Several literature studies have addressed heat transfer in the flow past heated circular cylinders. In particular, Nakamura and Igarashi (2004) and Sanitjai and Goldstein (2004) have studied a wide range of Reynolds numbers ($70<Re<105$) and reported the Nusselt number variations. In the regime where the flow remains two-dimensional Bharti et al. (2007) and Vegad et al. (2014) investigated the heat transfer of steady flows ($Re<47$), while Patnana et al. (2010), Baranyi (2003), Golani and Dhiman (2014) and Harimi and Saghafian (2011) examined the interaction of heat transfer and the Kármán vortex street in the unsteady flow regime ($47<Re<180$). In more specific, Nakamura and Igarashi (2004) suggested that in the Reynolds – Nusselt numbers correlation, inconsistencies are expected in the flow transition regimes. They demonstrated that a reverse correlation exist between the vortex formation length and the Nusselt number at the rear stagnation point region. As a result, the shortening of the vortex formation length occurring in the regime in which the wake develops to a complex three-dimensional flow ($300 < Re < 1500$) has a negative impact on the mean Nusselt number. However, in both two-dimensional steady and unsteady flow regimes ($Re<180$), it was demonstrated that the value of the mean Nusselt number increases monotonically with the increasing value of the Reynolds number. This occurs in the unsteady regime due to the formation of the vortex street (Baranyi L. 2003); the intensity of the vorticity reflects the increase of the heat transfer rate.

In the present study, a non- isothermal flow past a circular cylinder is investigated, for low values of Reynolds number ($40<Re<180$). In this region, Baranyi (2003), Harimi and Saghafian (2011) and Karniadakis (1987) identfied the general distribution of the local Nusselt number across the cylinder surface. They demonstrated that the maximal value of the local Nusselt number is attained at the front stagnation point ($\theta=0^{o}$) due to the thin boundary layer present at that point. As the boundary layer becomes thicker, the local Nusselt number decreases steeply and its minimal value is

observed in the regime between the separation point and the rear stagnation point ($90^o<\theta<160^o$). Further, a local maximum is observed at the rear stagnation point ($\theta=180$), which is due to the formation of the vortex shedding. Finally, although the maximum and local maximum values of the local Nusselt number increase with an increase of the Reynolds number, (Nakamura and Igarashi, 2004, Harimi and Saghafian, 2011) the minimum local Nusselt number value is unaffected, and thus remains constant (Harimi and Saghafian, 2011).

1.3.3 Heat transfer enhancement in wake flows

The problem of enhancing heat transfer, is a classical problem with great challenges in the fields of fluid mechanics and thermal engineering. Concerning the flow past a heated cylinder, several literature studies have addressed the problem of heat transfer enhancement, by means of both passive and active flow control techniques (see below section 1.4.1). Some of them include cylinder rotation (Pourgholam et al., 2015) or use of nanofluids (Bovand et al., 2015, Ziyad et al., 2008). In particular, Pourgholam et al. (2015) utilized the flow augmented agitation, in comparison to the stationary cylinder, which led on heat transfer enhancement. On the other hand, Bovand et al. (2015) and Ziyad et al (2008) achieved heat transfer enhancement by exploiting the addition of nanoparticles in the base fluid, leading to an increased effective dynamic viscosity and thermal conductivity. However, these methods deviate from the objectives of this study as they destabilize the global flow. Here, a method that enhances heat transfer, while at the same time suppresses the flow instability, is investigated. A possible candidate for heat transfer enhancement according to Haase et al (2015), Maynes et al. (2008) and Rothstein (2010) is the application of surface hydrophobicity. In flow through microchannels, Haase et al. (2015) and Maynes et al. (2008) demonstrated that the application of surface hydrophobicity involves two conflicting effects. On the one hand, the heat transfer coefficient is reduced due to the reduction of the liquid-solid contact, while, on the other hand, the reduction of the drag force coefficient, results in the increase of the local boundary velocities of the flow, amplifying the velocity profile and enhancing heat transfer. They have demonstrated that the second effect predominated the first one, and thus the heat transfer rate was enhanced.

1.4 Flow control

1.4.1 Flow control: suppression of unsteadiness

In flow past a cylinder several control strategies have been investigated, aiming at the suppression of the Kármán vortex street. The flow control methods are distinguished as passive or active, regarding the energy input they require after they have been set. In particular, the passive control methods usually include a geometry modification, such as (a) placement of a splitter plate (Roshko, 1955), (b) proper placement of a smaller cylinder in the wake (Strykowski and Sreenivasan, 1990, Mittal and Raghuvanshi, 2001, Yildirim et al., 2010) or (c) application of a hydrophobic material on the surface of the cylinder (You and Moin, 2007, Legendre et al. 2009, Muralidhar et al., Seo and Song, 2012 and Mastrokalos et al., 2015). On the other hand, the active control methods require an external energy input, as for example a (a) suction/blowing on the cylinder surface (Delaunay Y. and Kaiktsis L. 2001), (Wood CJ. 1967), (Dong et al. 2008), (b) cylinder rotation and/or rotary oscillation, (Tokumaru PT. and Dimotakis PE. 1991), (Tokumaru PT. and Dimotakis PE. 1993), (Mittal S. and Kumar B. 2003), (c) cylinder heating (Lecordier JC. 1991) or an (d) application of a Lorentz force (Chen Z. and Aubry N. 2003).

1.4.2 Implementation of surface hydrophobicity

Hydrophobic or superhydrophobic surfaces are bio-inspired surfaces, characterized by a combination of micro- and nanoscale roughness. Superhydrophobic surfaces are resistant to wetting, thus enabling low friction levels in fluid flows. Hydrophobicity is commonly quantified by the value of contact angle between a liquid drop and the surface, which in hydrophilic surfaces is less than 30 deg, in hydrophobic surfaces less than 150 deg and in superhydrophobic surfaces higher than 150 deg (Fig. 3). Macroscopically, use of hydrophobic surfaces may result in a deviation from the no-slip condition at the fluid boundary, resulting in the presence of a nonzero velocity at the boundary wall (slip velocity).
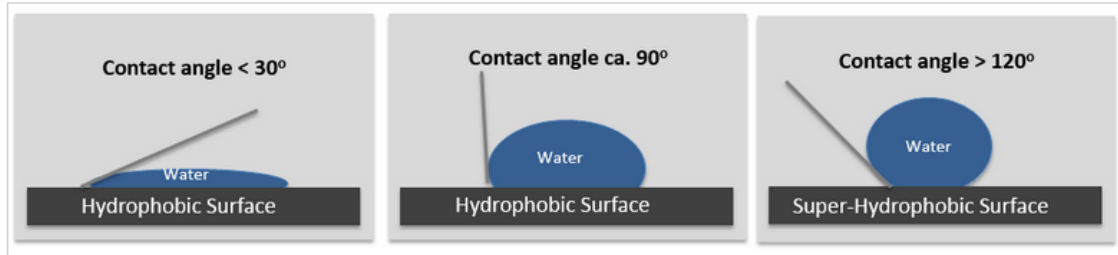
Fig. 3. Contact angle for: (a) hydrophilic surfaces, (b) hydrophobic surfaces and (c) superhydrophobic surfaces.

Implementation of hydrophobicity on the cylinder surface passively controls the flow supressing its unsteadiness. In particular, fluid slip at the cylinder surface leads to a delay of separation, and thus to the formation of a narrower wake. This reduces the intensity of the lift and the drag force oscillations (Legendre et al. 2009), and may even lead to a complete suppression of the vortex street (You and Moin 2007, Mastrokalos et al. 2015).

At the same time, as was earlier mentioned (*1.3.3*), the implication of hydrophobicity can enhance heat transfer between the cylinder and the fluid. The main question here is to investigate whether the vortex suppression, resulting in lower velocities at the rear stagnation point region, combined with the reduction of the liquid-solid contact (Haase et al 2015, Maynes et al. 2008 and Rothstein, 2010), can be counterbalanced by the increased boundary velocities due to hydrophobicity, in the remainder cylinder, and if, as a result, heat transfer can actually be enhanced.

Finally, it should be noted, that due to the substantial manufacturing cost of hydrophobic and superhydrophobic surfaces, the minimization of the extent of the hydrophobic region should be a main consideration.

1.5 Goal of the present study

In the present computational study hydrophobic materials are implemented on the entire cylinder surface or on a part of it, in order to achieve three goals, namely: (a) heat transfer enhancement, (b) partial or full suppression of the Kármán vortex street and (c) use of a minimal control effort (minimization of cost and of the extent of the hydrophobic region. At first, hydrophobicity is applied on the entire cylinder surface. The results demonstrate a substantial heat transfer enhancement in comparison to the uncontrolled case. However, it is highlighted that in the rear stagnation point region heat transfer is decreased, due to the increase of local velocities. Therefore, in a second step, hydrophobicity is

implemented on a part of the cylinder surface. It is verified that partial hydrophobicity can lead to the same levels of heat transfer as in the full slip case. Finally, guided, by these results a multi-objective optimization problem is formulated and solved, aiming at the maximization of heat transfer rate and the minimization of the flow unsteadiness and the control effort. The solution of the optimization problem by means of genetic algorithms results in optimal combinations of the slip length and the extent of the hydrophobic region. Here, the term optimal refers to the minimization/maximization of proper defined objective functions corresponding to the three goals defined above.

The present diploma thesis is organized as follows. In Chapter 2, the problem setup is presented. In Chapter 3, results of numerical simulations of flow past a cylinder with slip on the entire or part of its surface (full/partial slip) are presented and analyzed. In Chapter 4, the optimization problem of the present study is defined, and the optimization results are presented and discussed, for two values of Reynolds number. Finally, in Chapter 5, the main findings of the present thesis are summarized.

2. PROBLEM SETUP

2.1 Computational model – boundary conditions

We consider a circular cylinder in uniform cross-flow. In the present study, the thermo-physical properties of the fluid are assumed to be independent of the temperature. The variable-density effects are negligible and the specific heat capacity, C_P, and the thermal conductivity, k, of the fluid are constant, thus the energy of the fluid per unit mass can be expressed as $de_{steam} = dh = C_P dT$ and the energy equation takes the following form (12). As a result, the temperature difference between the cylinder, T_w, and the free steam, T_{inf}, is maintained small so that these simplifying assumptions can be justified. Flow fields are computed from the numerical solution of the non-dimensional Navier–Stokes equations for two-dimensional incompressible non-isothermal flow:

$$\text{Continuity equation:} \qquad \nabla \cdot \vec{u} = 0 \qquad\qquad (10)$$

$$\text{Momentum equation:} \qquad \frac{\partial \vec{u}}{\partial t} + \vec{u} \cdot \nabla \vec{u} = -\nabla p + \frac{1}{Re} \Delta \vec{u} \qquad (11)$$

$$\text{Energy Equation:} \qquad \frac{\partial T}{\partial t} + \nabla \cdot (\vec{u} T) = \frac{1}{Re \cdot Pr} \Delta T \qquad (12)$$

where $\vec{u} = (U, V)$ is the velocity vector and p the static pressure and T is the temperature. Here, physical variables are non–dimensionalized with proper scales based on the cylinder diameter, D, the free stream velocity, U_{inf}, the fluid density, ρ, the cylinder's wall temperature, T_w and the free steam temperature, T_{inf}. Frequencies are non- dimensionalized as Strouhal numbers, $St = \dfrac{fD}{U_{inf}}$. The Reynolds number is defined as $Re = \dfrac{U_{inf} D}{\nu}$, where ν is the kinematic viscosity of the fluid, and the Prandtl number as $Pr = \dfrac{\mu \cdot C_P}{k}$, where μ is the dynamic viscosity of the fluid, C_P the specific heat capacity and k the thermal conductivity.

The numerical solution of the governing equations utilizes the ANSYS CFX CFD code. Here, a second-order finite volume approach is adopted.

The center of coordinates (x=0, y=0) is taken at the cylinder center. The following conditions are prescribed at the domain boundaries (see Fig. 4).

Inflow and lateral boundaries: $U = U_{inf} = 1,\quad V = 0,\quad T = T_{inf} = 0$

Outflow boundary: $p=0$, Neumann boundary condition

Cylinder surface: $u_\theta = \tau b^* Re = b^* \dfrac{\partial u_\theta}{\partial r},\quad u_r = 0,\quad T = T_W = 1$ (Navier model, Zhang et al., 2012)

where u_θ and u_r are the non-dimensional velocity components in the circumferential and radial direction, respectively (see Fig. 5), τ is the non-dimensional wall shear stress and b^* is the non-dimensional slip length. The Navier model thus assumes that the fluid flows against a fictitious (non-hydrophobic) surface, located at a distance b from the actual solid boundary (slip length, see Fig. 5). Slip velocity at the cylinder surface is proportional to the local values of shear stress and slip length. In the present study, the value of slip length is assumed constant for the entire hydrophobic part of the cylinder surface.

Furthermore, heat transfer is quantified by the non-dimensional Nusselt number and the cylindrical cylinder is maintained at the constant temperature of T_w. The local Nusselt number, $Nu(\theta)$, on the surface of the cylinder is defined as:

$$Nu(\theta) = \frac{h_c \cdot D}{k} \tag{13}$$

Here, h_c is the local value of the convective heat transfer coefficient calculated as:

$$h_c = -\frac{k(\partial T / \partial \vec{n})\big|_w}{(T_w - T_{inf})} \tag{14}$$

where $\vec{n}$ is the direction normal to the cylinder. The mean Nusselt number, defined as the overall surface average value of the local Nusselt number, is obtained by integrating $Nu(\theta)$ over the surface of the cylinder, as follows:

$$Nu_m = \frac{1}{2\pi} \int_0^{2\pi} Nu(\theta) d\theta \tag{15}$$

whereas the time-averaged mean Nusselt number is calculated as:

$$\overline{Nu_m} = \frac{1}{t_p} \int_0^{t_p} Nu_m dt \tag{16}$$

For stable solutions, the mean Nusselt number attains a constant value, while for unstable solutions an oscillatory behavior corresponding to limit cycle is observed.

For the present problem, it follows from dimensional analysis that the flow dynamics depends (i) on the Reynolds number, *Re*, (ii) on the Prandtl number, *Pr* and (iii) on the non-dimensional slip length, *b**. Here, results are presented for the representative value of the Prandtl number, *Pr*=1 and for four values of Reynolds number, *Re*= 40, 90, 120, 150, 180, for which the uncontrolled flow is unsteady and two-dimensional.
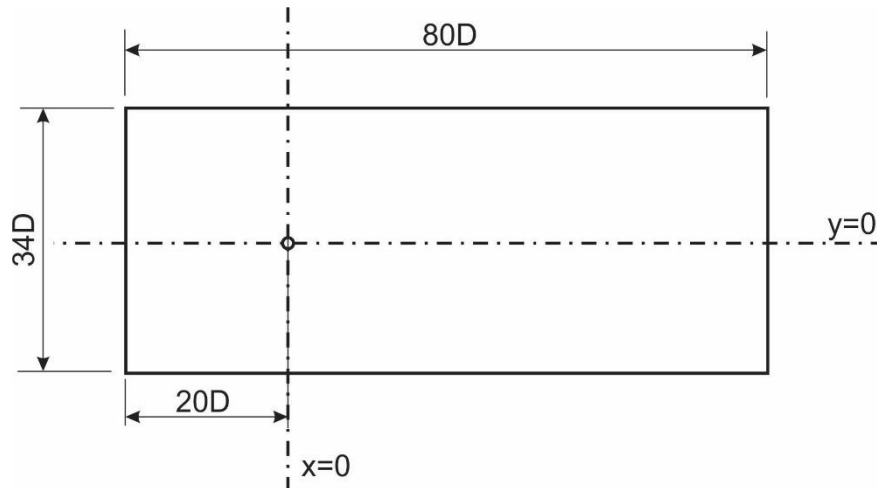
Fig. 4. Flow domain.
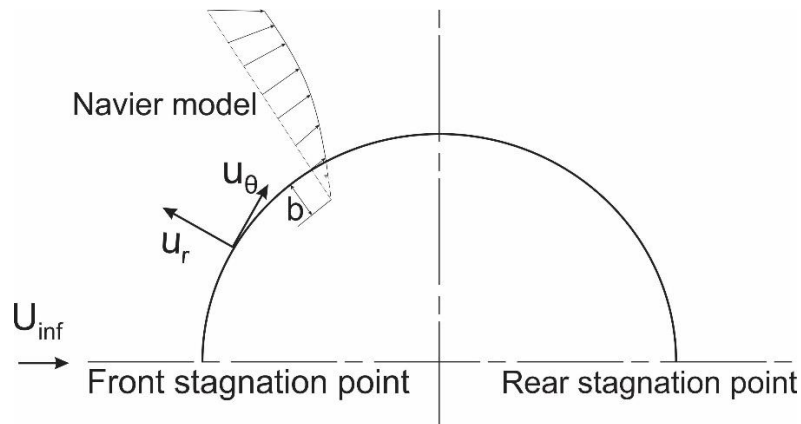
Fig. 5. Sketch of velocity profile near cylinder surface, for a slip length *b*.. Local velocity components on the cylinder surface, u_θ and u_r are depicted.

2.2 Domain definition – grid generation

The computational domain extends *20D* upstream from the cylinder center and *60D* downstream, while the lateral boundaries lie *17D* from *y*=0, the domain centerline (Fig. 4). The adequacy of this domain size has been demonstrated in relevant literature studies (see Kaiktsis et al., 2007,

Delaunay and Kaiktsis, 2001 and Evangelinos and Karniadakis 1999). Spatial resolution tests have shown that a grid with 54000 quadrilateral finite volumes, with approximately 100 volumes osculating to the cylinder surface (see Fig. 6), is sufficient for the Reynolds number range of the present study. A time step value of 0.01 non-dimensional time units has been used throughout the present study, and its adequacy is verified by temporal resolution tests utilizing smaller time step values (up to 0.005 time units).
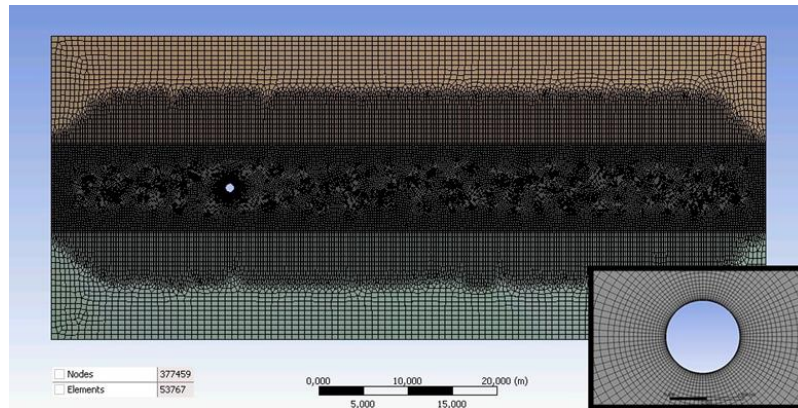
Fig. 6. Finite volume mesh with detail close to the cylinder (the number of finite volumes osculating to cylinder surface is close to 100).

2.3 Validation tests

The present CFD results are validated by comparing high resolution simulations of the uncontrolled flow against published literature data. Here, the simulations are performed for the Reynolds number range between *Re*=10 and *Re*=180, for which the flow remains two-dimensional. In particular, the distribution of the local Nusselt number for the present study is presented and compared with that of Patnana V. et al. (2010) in Fig. 7a. Further, in Fig. 7b the mean Nusselt number for different Reynolds number values is compared with the calculations of Patnana V. et al. (2010), as well as with the ones of an empirical correlation; an excellent agreement between the present and the literature and empirical results is demonstrated.
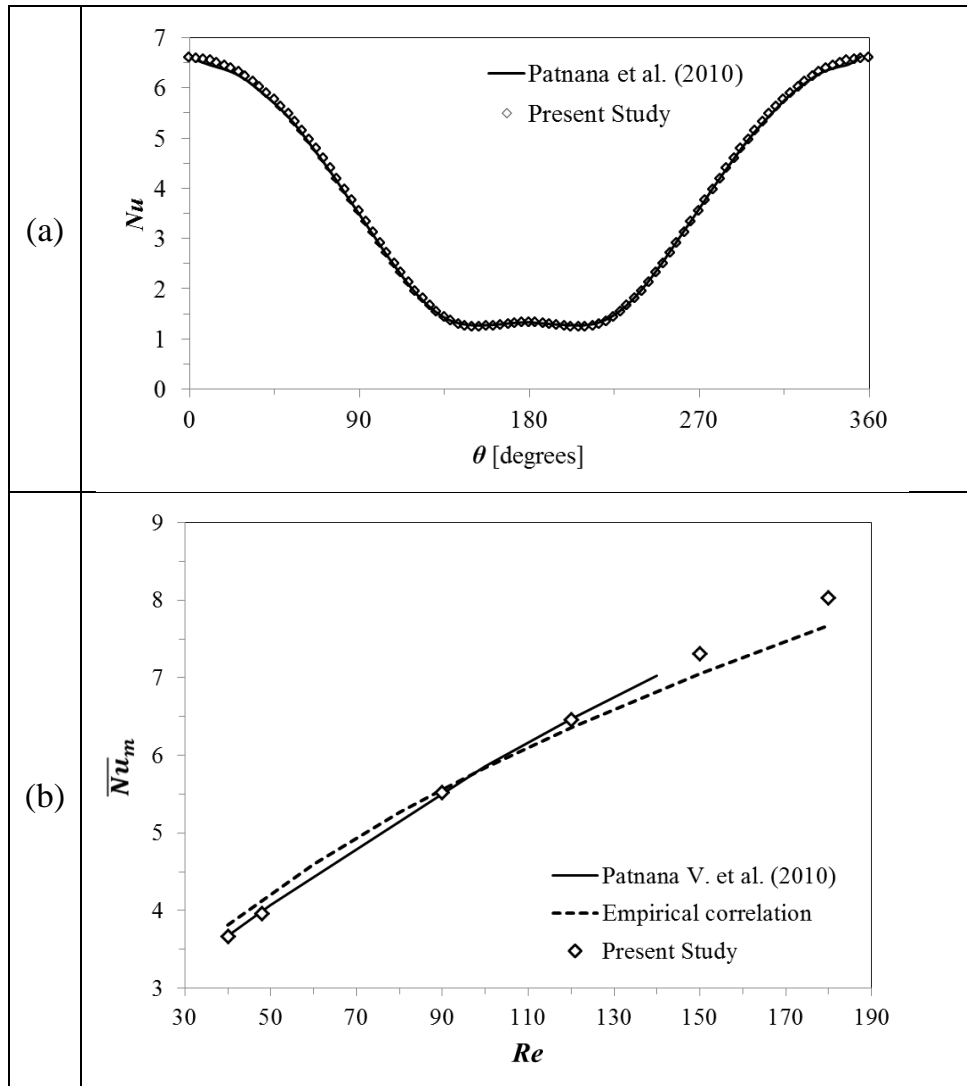
Fig. 7. Validation of the present study results with literature studies: (a) local Nusselt number for *Re*=40, (b) time-averaged mean Nusselt number for representative values of Reynolds number.

3. COMPUTATIONAL RESULTS

3.1. Application of slip conditions on the entire cylinder surface

3.1.1 Application of full slip at a constant value of slip length for various Reynolds number values

For given Reynolds number values (Re=40, 90, 120, 150 and 180), flow and temperature fields have been computed for the uncontrolled flow, as well as for a hydrophobic case at the non-dimensional slip length value b^*=0.2; in the latter hydrophobicity is applied on the entire cylinder surface. For all cases considered, Fig. 8 presents the time-averaged local Nusselt number values along the cylinder surface, whereas Fig. 9 and Fig. 10 illustrate the instantaneous vorticity and temperature isocontours respectively.

In the uncontrolled case (b^*=0), Fig. 9i demonstrates the presence of the recirculation zone for Re=40 and the formation of the Kármán vortex street for Re=90, 120, 150 and 180. The structure of the vortex shedding is in accordance with the structure of the temperature isocontours (Fig. 10i). For the same case, concerning the distribution of the local Nusselt number, it is verified, that its maximal value is attained at the front stagnation point (θ=0°), while the corresponding lowest value is reached between the separation point and the rear stagnation point (Fig. 8). Moreover the local Nusselt number attains a local maximum at the rear stagnation point, which is due to the high velocities created by the vortex shedding. It is also demonstrated, that an increase of the Reynolds number results in an increase of the local Nusselt number in the rear stagnation point and more intensively in the front stagnation point.

When slip conditions are applied on the entire cylinder surface (b^*=0.2), the Kármán vortex street is fully canceled for Re=40, 90, 120 and partially suppressed for Re=150 and 180 (Fig. 9ii); a similar behavior is observed in the corresponding temperature isocontours (Fig. 10ii). The distribution of the local Nusselt number demonstrate, that for Re=90, 120, 150 and 180 (Fig. 8b-e), its minimum values are located closer to the rear stagnation point, in comparison with the uncontrolled cases. This observation demonstrates, that when the vortex street is cancelled, the two minimum values of local Nusselt number tend to merge into one, as seen for Re=40 (Fig. 8a) where the minimum value of local Nusselt number is located in the rear stagnation point.

In general, by comparing controlled against uncontrolled cases, it is demonstrated (Fig. 8) that the local Nusselt number increases in the front stagnation point region, but decreases in the rear stagnation point region. In more detail, the local Nusselt number reduction in the rear stagnation point region is caused by the suppression of the vortex street, while in the rest of the cylinder, and more prominently in the front stagnation point region, due to the presence of hydrophobicity. Further, the area which is affected negatively regarding the heat transfer, close to the rear stagnation point, is much smaller in comparison to the enhanced one in the rear stagnation point region.

Furthermore, Fig. 11 presents the calculated values of the mean Nusselt number for all the cases considered. It demonstrates an increase of the mean Nusselt number by the application of hydrophobicity, verifying the earlier observations concerning the local Nusselt number. It should be noted, that the increase in the mean Nusselt number is stronger for larger Reynolds number values; the latter is due to an increase of local velocities in the rear stagnation point region, leading to a corresponding increase in heat transfer.

The earlier analysis suggests that the stabilization of the flow has a negative impact on the heat transfer enhancement, affecting in particular the rear stagnation point region. However, this comes as an inevitable result of the application of slip which leads to substantial heat transfer enhancement in the remaining part of the cylinder i.e. all the cylinder surface excluding a region near the rear stagnation point. Finally, Table 1 summarizes the time-averaged mean Nusselt number values of the uncontrolled flow, as well as those of the controlled flow (b^*=0.2), for various Reynolds numbers, and the corresponding heat transfer enhancement of the controlled flow. It is demonstrated that up to 31% improvement in the heat transfer rate can be achieved, which is similar to the heat transfer enhancement Maynes et al.(2008) calculated in their work regarding flow in a microchannel with hydrophobic surface.
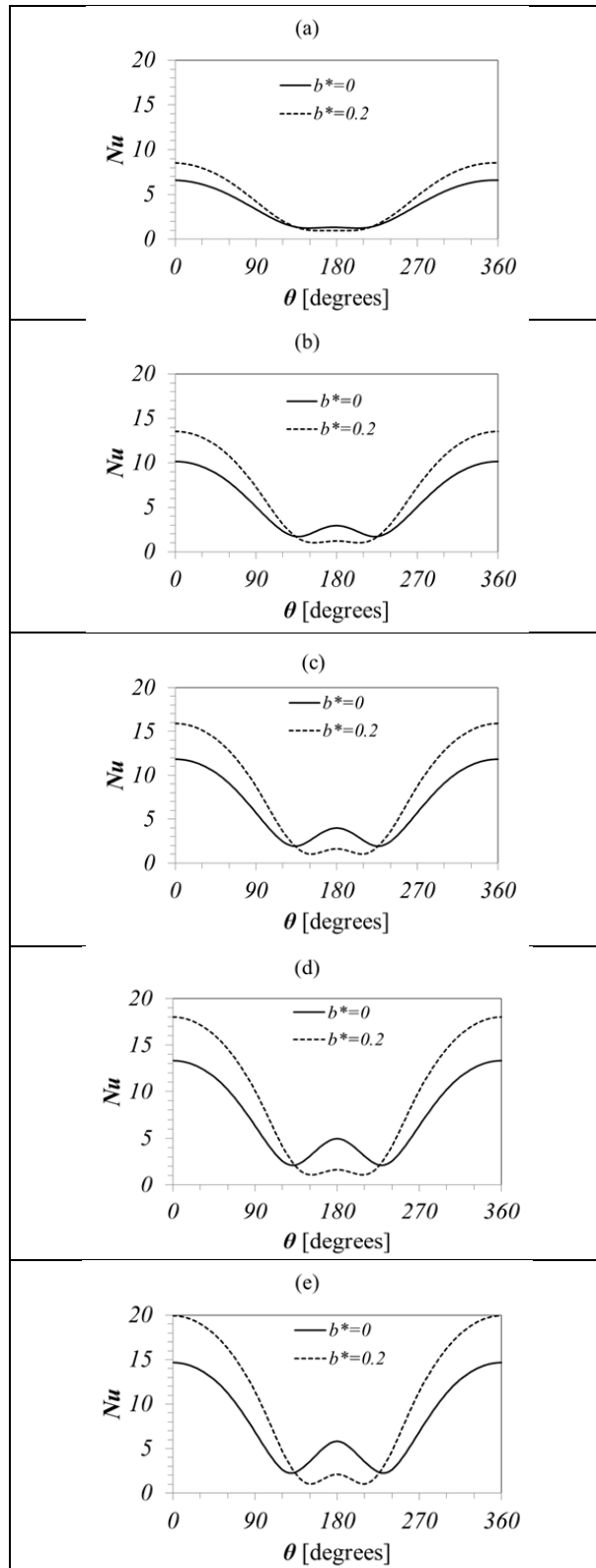
Fig. 8. Local Nusselt number distribution for (i) uncontrolled flow ($b*$=0) and (ii) for controlled flow at $b*$=0.2 for the Reynolds numbers: (a) Re=40, (b) Re=90, (c) Re=120, (d) Re=150 and (e) Re=180; the front stagnation point is considered as the reference point (θ=0°).
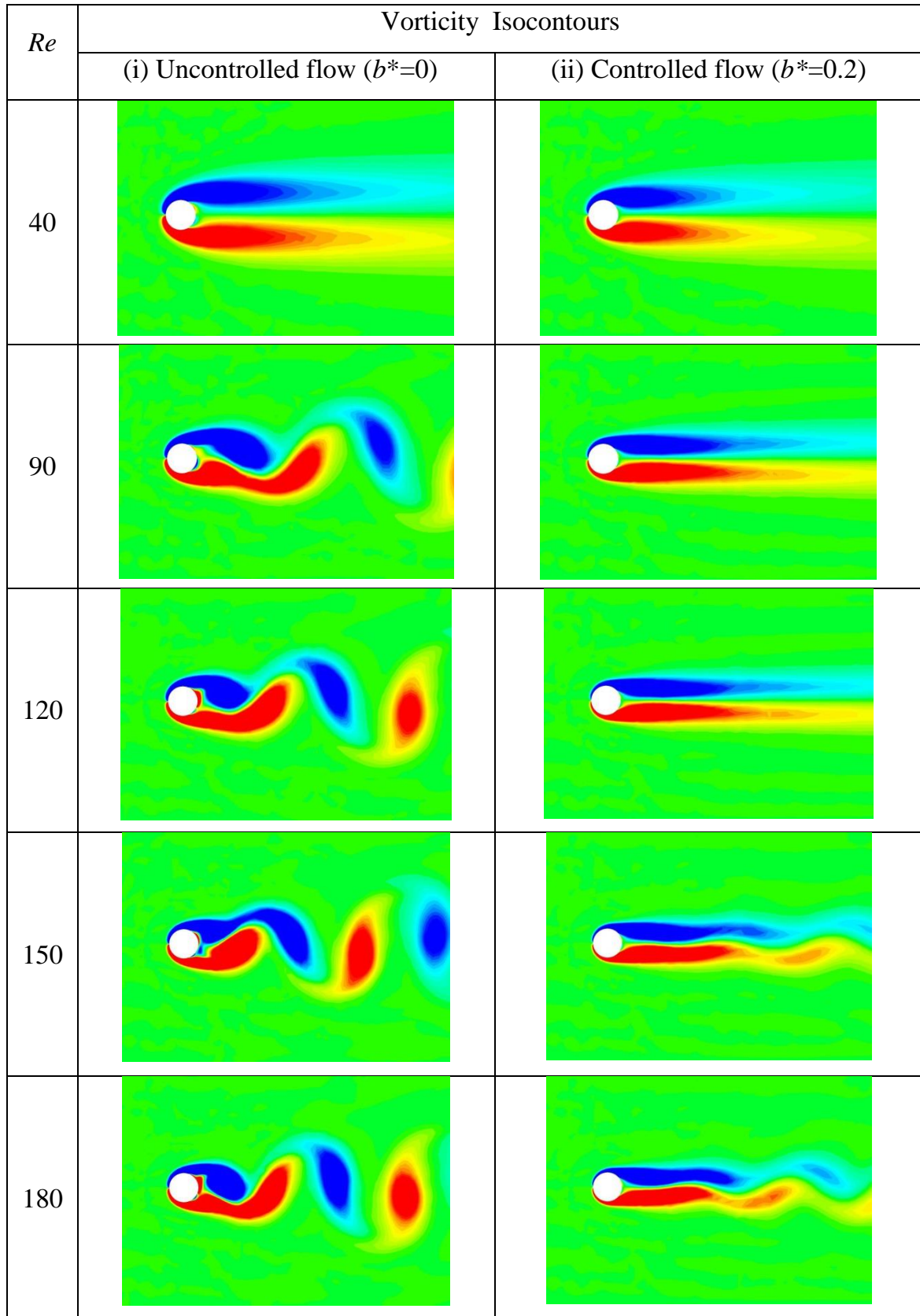
Fig. 9. Color-coded contours of instantaneous vorticity for representative Reynolds number values, corresponding to (i) Controlled and (i) Uncontrolled cases, in the non-linear flow state.

Re	Temperature Isocontours	
	(i) Uncontrolled flow ($b*=0$)	(i) Controlled flow ($b*=0.2$)
40		
90		
120		
150		
180		
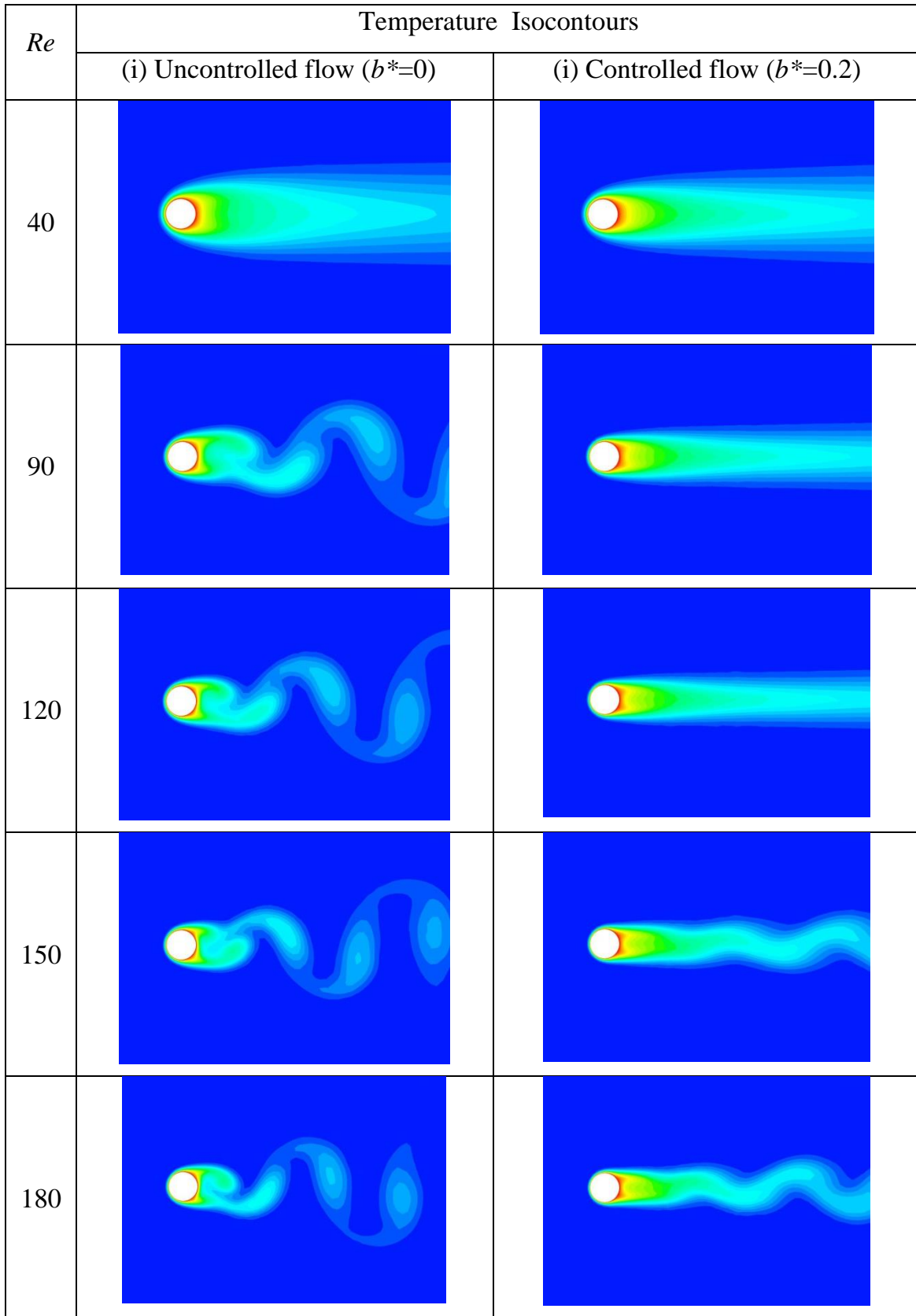
Fig. 10. Color-coded contours of instantaneous temperature for representative Reynolds number values, corresponding to (i) Controlled and (i) Uncontrolled cases, in the non-linear flow state.
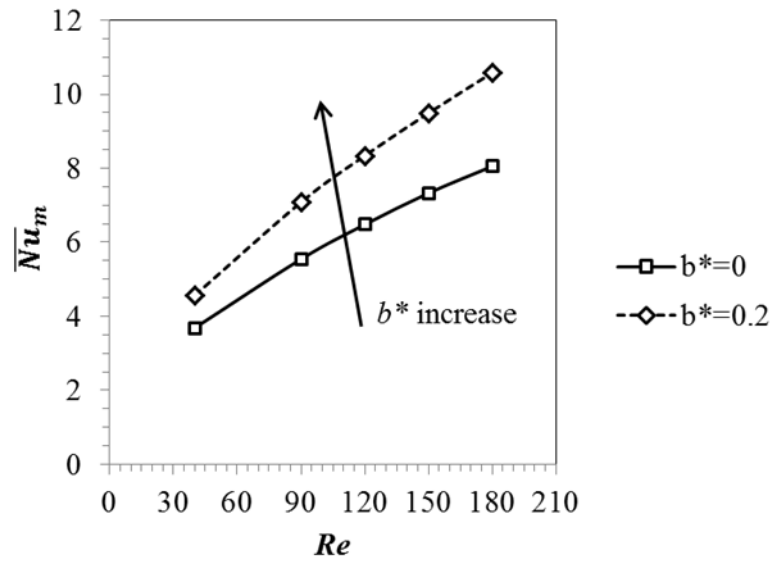
Fig. 11. Time-averaged mean Nusselt number vs Reynolds number for (i) uncontrolled flow ($b^*=0$) and (ii) for controlled flow at $b^*=0.2$

Table 1. Computed values of time averaged mean Nusselt number, at different values of Reynolds number, for: (i) uncontrolled flow, (ii) controlled flow at a specific value of non-dimensional slip length, $b^*=0.2$.

Re	$\overline{Nu}_m$		Heat transfer Enhancement (%)
	(i) $b^*=0$	(ii) $b^*=0.2$	
40	3.6858	4.5641	23.8
90	5.5443	7.0821	27.7
120	6.4796	8.3405	28.7
150	7.3281	9.4913	29.5
180	8.0539	10.5824	31.4

3.1.2 Application of full slip at a given Reynolds number value for various values of slip length

In order to investigate in more detail the effect of hydrophobicity on heat transfer, computational calculations were performed for a sufficiently large range of b^* values, at the representative Reynolds number value, $Re=90$.

Fig. 12 presents the time-averaged mean Nusselt number as a function of the non-dimensional slip length, b^* whereas, Fig. 13 and Fig. 14, present the vorticity and temperature isocontours for unstable and stabilized flow respectively. As the slip length increases, the vorticity intensity is reduced (Fig. 13) up to the limit of vortex street cancelation at the critical value of $b^*=0.17$; the latter is in excellent agreement with Legendre et al. (2009) and Mastrokalos et al. (2015). A further increase in b^* results in a reduction of the recirculation zone length (Fig. 14). Moreover, regarding heat transfer, it is shown that an increase of b^* results in an increase of $\overline{Nu_m}$. In Fig. 12 it is illustrated that the gradient of the curve remains considerable for small to moderate values of b^*; this region includes both stable and unstable solutions. As a result, hydrophobicity is more efficient for small to moderate values of b^* i.e. for $b^*<0.3$. On the other hand, for $b^*>0.3$ hydrophobicity becomes ineffective, as for example doubling the value of b^* returns slight increase of $\overline{Nu_m}$; the latter is also verified by the fact that for $b^*>0.3$ the temperature isocontours attain negligible deviations (Fig. 14).
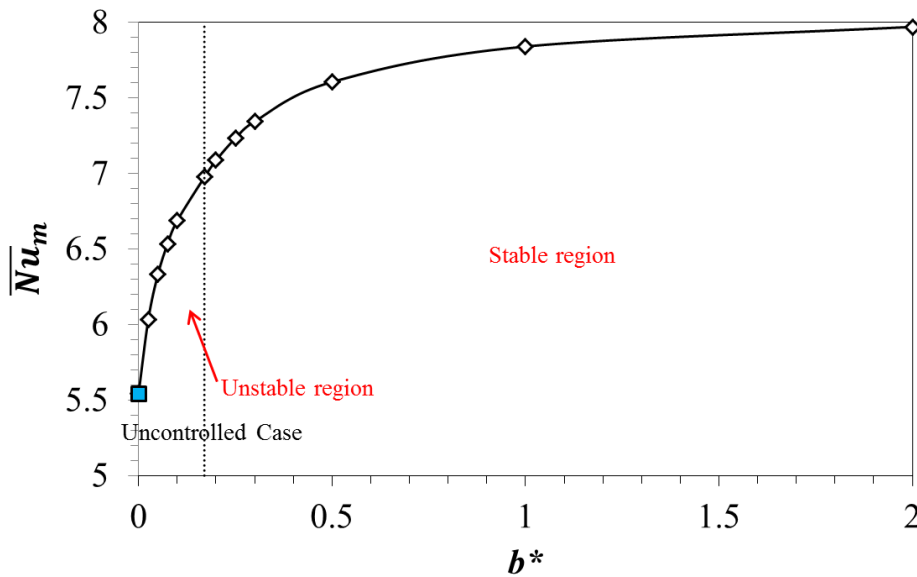
Fig. 12. $Re=90$:Time-averaged mean Nusselt number vs. non-dimensional slip length, b^*.
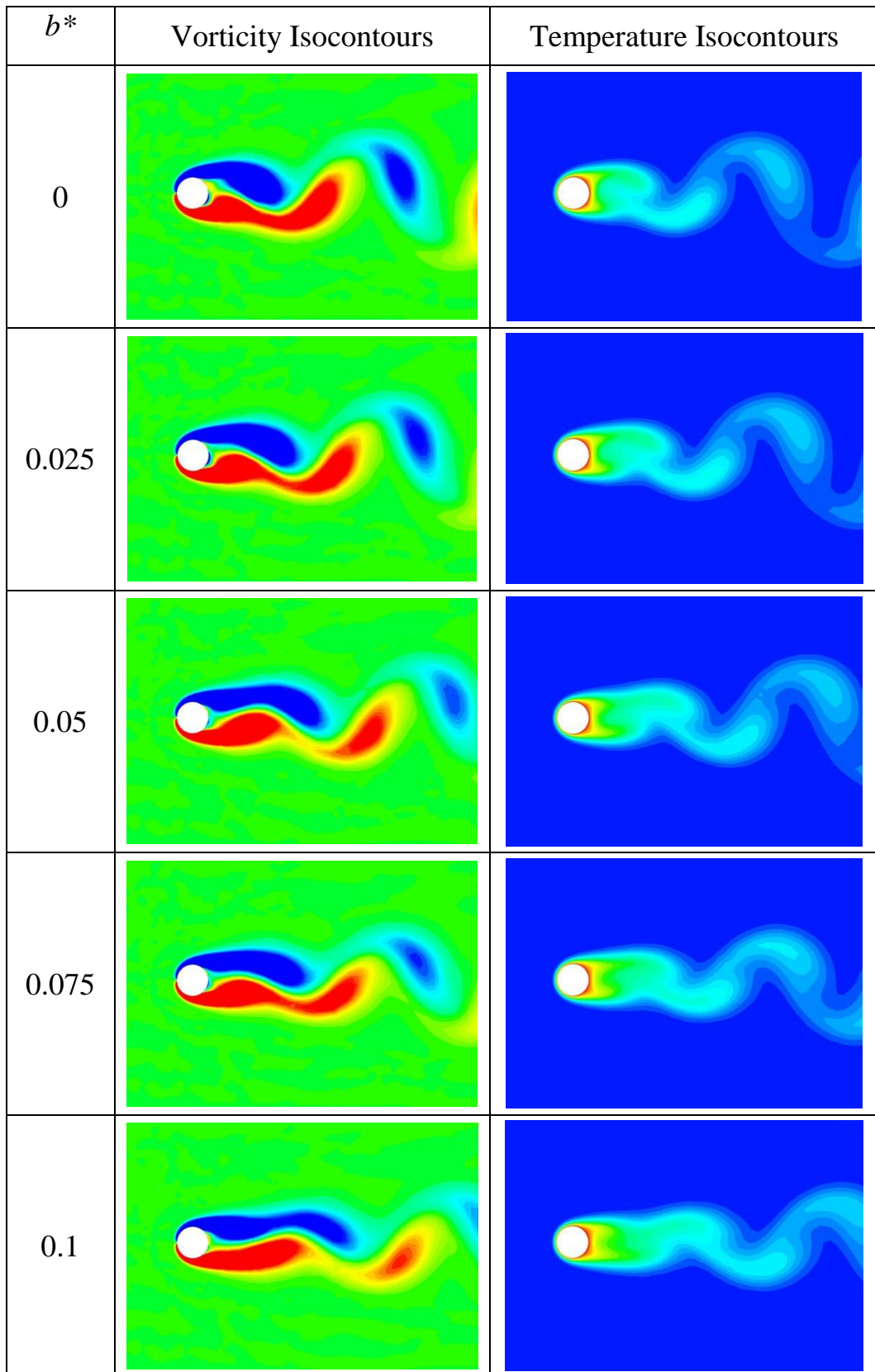
Fig. 13. *Re*=90: color-coded contours of instantaneous vorticity (left column) and color-coded contours of instantaneous vorticity (right column) in the non-linear flow state, corresponding to unstable cases depicted in Fig. 12.

$b*$	Vorticity Isocontours	Temperature Isocontours
0.17		
0.2		
0.3		
0.5		
2		
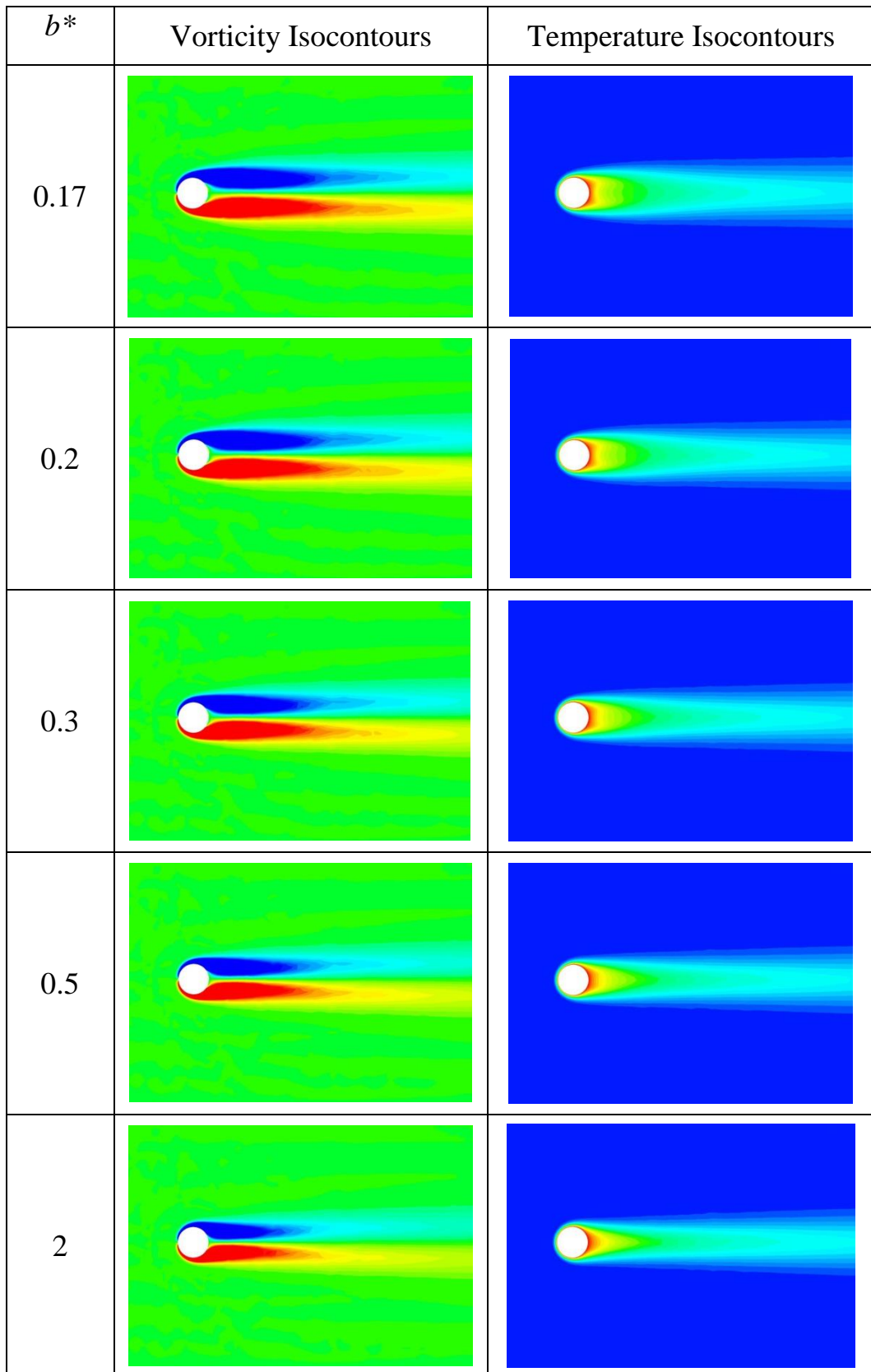
Fig. 14. *Re*=90: color-coded contours of instantaneous vorticity (left column) and color-coded contours of instantaneous vorticity (right column) in the non-linear flow state, corresponding to stable cases depicted in Fig. 12.

3.2. Application of slip conditions on part of the cylinder surface

When hydrophobicity is applied correctly on a part of the cylinder, disabling slip in the region of the rear stagnation point, it was shown (Mastrokalos et al. 2015), that the flow can be stabilized even more compared to the full slip case. In section 3.1 it was demonstrated that the suppression of the vortex shedding causes heat transfer to hinder in the region of the rear stagnation point, however the mean Nusselt number is slightly affected, when the suppression is achieved by means of hydrophobicity. The main goal here is to investigate whether the control effort, defined by the product of the non-dimensional slip length, b^* and the extent of the hydrophobic regime, can be substantially reduced, while in the same time achieving equivalent heat transfer enhancement in comparison with the full slip case.

To this end, the cases of full and partial slip are investigated and compared. Here, simulations are performed for Re=90 for the representative value of non-dimensional slip length b^*=0.17, which corresponds to global flow stabilization at Re=90, when slip is applied on the entire cylinder surface. In the partial slip case, slip conditions are applied on the entire cylinder surface excluding a region extending $\pm32^{\circ}$ from the rear stagnation point. Provided that the non-dimensional slip length, b^*, is the same for both cases, the control effort depends only on the extent of the hydrophobic region, defined by the angles θ_{min} and θ_{max} (Fig. 15).

Fig. 16 demonstrates that despite considerably decreasing the extent of the hydrophobic region, φ, and thus the control effort by 17.8%, the mean Nusselt number attains practically the same value as in the full slip case. At the same time, it is observed that the flow is stabilized quicker, which verifies the fact that the partial slip can be even more effective than full slip in suppressing the global flow instability.

Overall, these results suggest that an optimal partial slip setup should be examined more thoroughly with respect to the global flow stability and the heat transfer enhancement. As a result a proper optimization method should be addressed. To this end, a multi-objective optimization problem is formulated and solved, aiming at the maximization of heat transfer rate and at the identification of optimal combinations of the slip length and the extent of the hydrophobic region.
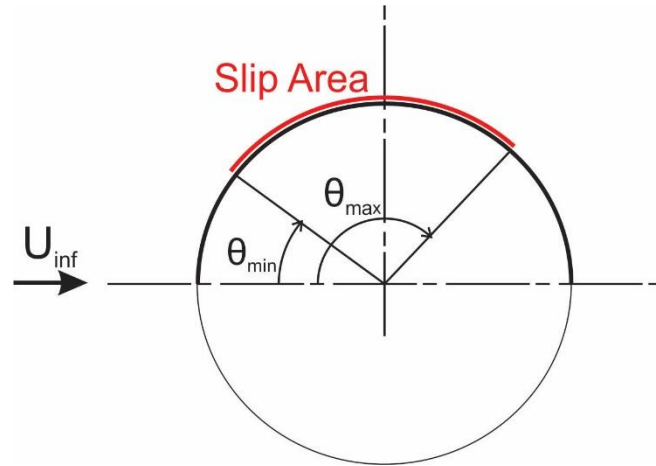
Fig. 15. Sketch of slip condition application on the cylinder surface, for a flow from left to right: slip is applied in the arc ranging from θ_{min} to θ_{max}.

Case	$\overline{Nu}_m$	Lift Signal
(i) Full Slip $\theta_{min}=0^o$ $\theta_{max}=180.0^o$ $\varphi=180^o$	6.97427	
(ii) Partial Slip: $\theta_{min}=0^o$ $\theta_{max}=148^o$ $\varphi=148^o$	6.97272	

Fig. 16. Computed values of time-averaged mean Nusselt number and lift coefficient signal, for *Re*=90 and *b**=0.17 for two cases: (i) full slip, (ii) partial slip.

4. FORMULATION AND SOLUTION OF OPTIMIZATION PROBLEM

The main goal of the present computational study is the heat transfer enhancement with complete suppression or intensity reduction of the Kármán vortex street in flow past a cylinder, by means of a proper implementation of partial slip. The partial slip parameters consist of the corresponding cylinder arc, defined by θ_{min} and θ_{max} (see Fig. 15), and the corresponding slip length, b^*. Here, an optimal passive control is sought, associated with attaining desired flow states at a minimal control effort. To this end, a three-objective minimization problem is formulated. The first objective function is associated with the flow's global stability. The second one quantifies the control effort, taking into account the slip length, b^*, and the extent of the slip region, which corresponds to the angle $\varphi=\theta_{max}-\theta_{min}$. Finally, the third objective function quantitatively expresses heat transfer, using the non-dimensional time-averaged Nusselt number. Optimization results are reported for two values of Reynolds number, $Re=90$ and $Re=180$.

4.1. Design variables and search space

Three design variables are utilized in the present implementation: the non-dimensional slip length, b^*, and the angles θ_{min} and θ_{max}, defining the slip area. The application of slip is symmetrical with respect to the domain centerline ($y=0$). A broad domain of definition is considered for each of the three design variables:

$$0 \le b^* \le 0.5 ,\ 0 \le \theta_{\min} \le 70^{o} ,\ 110^{o} \le \theta_{\max} \le 180^{o} \tag{17}$$

The selection of search space boundaries was guided by the simulations reported in Section 3, corresponding to implementation of full and partial slip.

4.2 Objective functions

Three objective functions are introduced.

(a) First objective function, J_1:

The first objective function, J_1, is related to the flow's global stability. Here, a total of M points along the domain centerline ($y=0$) is considered, and the numerical signal of the transverse velocity (V-component) at large times is analyzed, for each point. For a total of N data points in time (N being a very large number, corresponding to several flow periods), the objective function J_1 is defined as the average of the standard deviation values, S_j, of the V-velocity signals, in the population of M points:

$$\overline{V_{x_j}} = \frac{1}{N}\sum_{i=1}^{N} V_{t_i,x_j} \tag{2}$$

$$S_j = \sqrt{\frac{1}{N-1}\sum_{i=1}^{N}\left(V_{t_i,x_j} - \overline{V_{x_j}}\right)^2} \tag{3}$$

$$J_1 = \frac{1}{M}\sum_{j=1}^{M} S_j \tag{4}$$

where V_{t_i,x_j} is the transverse velocity at point x_j calculated at time instant t_i, $\overline{V_{x_j}}$ the corresponding time-averaged value, and S_j its standard deviation at point x_j. In the present study, $M=100$, corresponding to equidistant points in the wake region $1<x/D<21$.

Unsteady wakes are characterized by non-zero instantaneous V-velocities along the wake centerline, with the magnitude of velocities being representative of the intensity of the global mode. On the other hand, steady wakes are symmetric along their centerline ($V=0$). Thus, the value of J_1 is expected to decrease for control actions corresponding to increased stabilizing effects, becoming zero for steady flow.

(b) Second objective function, J_2:

The second objective function, J_2, defines the control effort, which increases with both the non-dimensional slip length, b^*, and the normalized half-arc of the slip region. Thus, their product is taken as the objective function J_2:

$$J_2 = b^* \frac{(\theta_{max} - \theta_{min})}{2} = \frac{1}{2} b^* \varphi \tag{5}$$

where $\varphi = \theta_{max} - \theta_{min}$ is expressed in radians.

(c) Third objective function, $\overline{Nu_m}$:

The third objective function, related to the heat transfer from the cylinder to the fluid, is the time-averaged mean Nusselt number, defined in eq. 7.

4.3 Optimization problem

The optimization problem is stated as follows: find the optimum combinations of the problem design variables (b^*, θ_{min}, θ_{max}), which simultaneously minimize objective functions J_1, J_2 and maximize the objective function $\overline{Nu_m}$. The optimization problem, as formulated here, is solved for two representative values of Reynolds number, Re=90 and Re=180, i.e. in a Reynolds number regime where the flow is two-dimensional.

4.4. Optimization methods

The final set of optimal solutions for the three-objective minimization/maximization problem of the present study is obtained by evolving, by means of a genetic algorithm, an initial, randomly generated, population (generation). The evolution produces subsequent generations, by utilizing the operations of parent selection, cross–over and mutation (see Fonseca and Fleming,1995). In the present work, each individual corresponds to a different slip condition (b^*), applied on a different part of the cylinder surface (defined by the two arcs, θ_{min} and θ_{max}), and is rated based on the resulting values of the problem objective functions. Here, the evaluator, finally giving the values of objective functions, is the CFD code ANSYS CFX, which is coupled to an optimization tool; the latter utilizes the ParadisEO genetic algorithms library (Cahon et al., 2004), and adopts the Non–dominated Sorting Genetic Algorithm NSGA-II for ranking solutions within a generation (Deb et al., 2002). The process terminates when the optimal set of solutions is hardly improved from one generation to the next. The final set of optimal solutions forms the problem's Pareto front; with respect to these solutions, there exist no others improving all of the problem objective functions. The optimization procedure is outlined in Fig. 17.

In the present implementation, each generation consisted of 20 individuals. Each optimization problem converged to the final Pareto front

after 22 generations. An individual CFD run has required approximately 12 hours of turnaround time, on 24 cores of a parallel cluster.
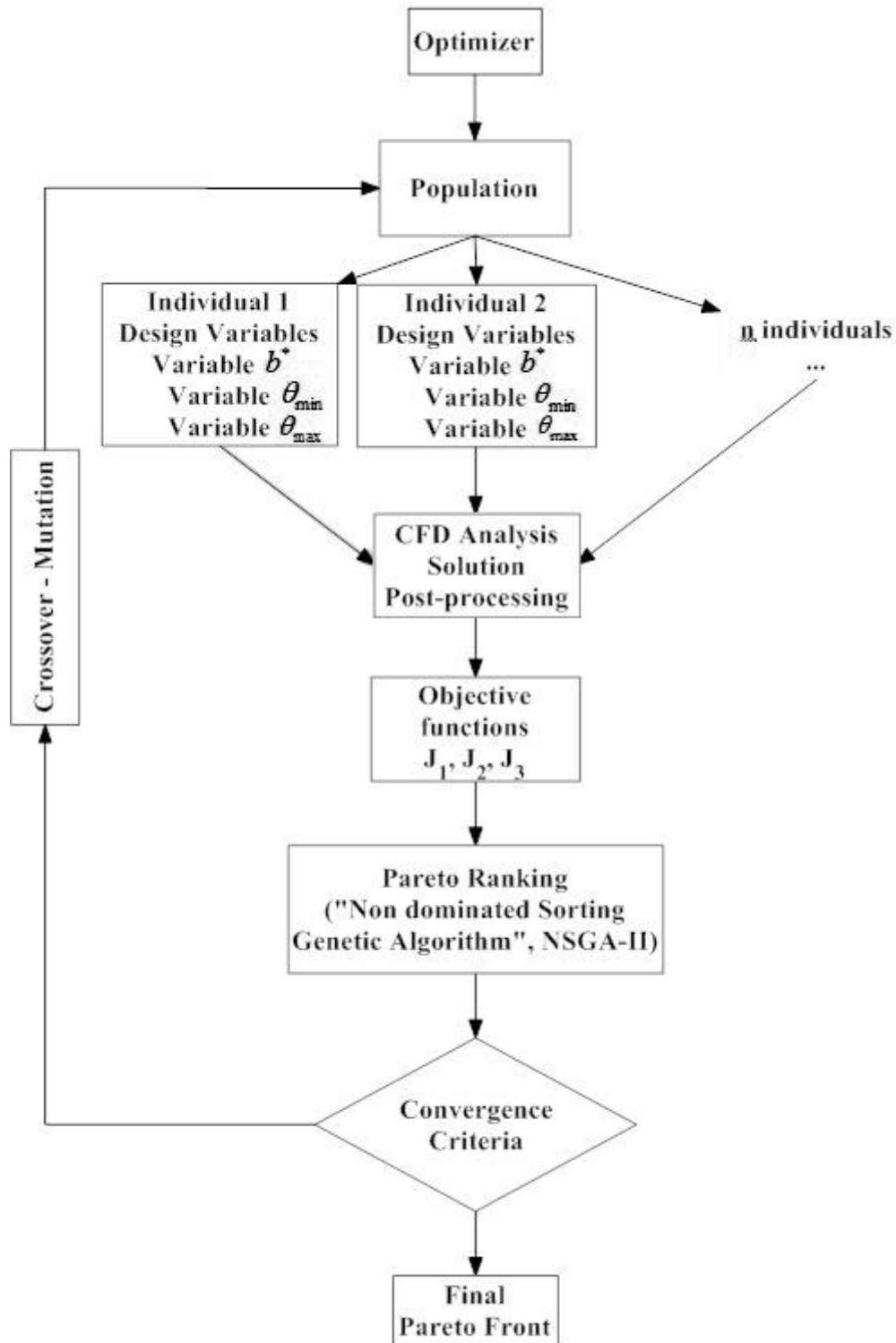

Fig. 17. Optimization flow chart.

4.5. Optimization results

4.5.1 Optimization results for Re=90

The optimization results for $Re=90$ are presented in Fig. 18, in terms of the values of the problem objective functions, J_1, J_2 and $\overline{Nu_m}$. Each combination of the problem design variables (b^*, θ_{min}, θ_{max}) corresponds to a different slip condition, resulting in either unstable or stable flow (values of function J_1 positive or zero, respectively). To obtain a better perspective of the optimization results Fig. 19, Fig. 20 and Fig. 21 were created by projecting the solutions at the level defined by the two objective functions considered; the red lines, depicted in those Figures, correspond to a virtual Pareto front, including all the non-dominated solutions; the uncontrolled case and the case of full slip case, at the representative value of non-dimensional slip length b^*=0.17, have been also added. The increase of the time-averaged mean Nusselt number as well as the decrease in control effort (J_2 value) of corresponding optimal flow cases in comparison with the full slip case are depicted in Fig. 19 and Fig. 20 respectively.

Specifically, in Fig. 19 the objective function J_1 is plotted versus the mean Nusselt number, $\overline{Nu_m}$. It is demonstrated that, in the set of optimal solutions, the increase of the flow stability results in higher heat transfer rate (increase of $\overline{Nu_m}$). Further, it is observed that a transition area exist around the value of mean Nusselt number $\overline{Nu_m} = 6.85$, separating unstable with stable solutions. This value is an upper limit value for unstable solutions, while for the stable ones $\overline{Nu_m}$ can increase even more reaching the value of the optimal solution, regarding the mean Nusselt number, Point e ($\overline{Nu_m} = 7.54497$). This optimal solution has a mean Nusselt number 75% higher in comparison with the full slip case (b^*=0.17), however, a much greater control effort is utilized. Namely for Point e the value of the objective function J_2 is 0.638, as for the full slip case J_2=0.267.

Moreover, in Fig. 20 the objective function J_1 is plotted versus the objective function J_2. It is displayed that in the set of optimal solutions, an increase in control effort results in a more stable flow (decrease of J_1). Point d represents the optimal solution giving global flow stabilization at a minimum control effort. Although Point d has a slip length value of b^*=0.174, which is relatively close to the one corresponding to stabilization with full slip (b^*=0.17), the extent of the hydrophobic region is significantly shorter, thus a reduction in control effort of 34% is demonstrated.

Finally, in Fig. 21 the objective function J_2 is plotted versus the mean Nusselt number. It is displayed that in the set of optimal solutions, an increase in control effort results in an increase of the mean Nusselt number. However, in correlation with *Section 3.1.1*, it is shown that exceeding a certain value of J_2 (about $J_2 \approx 0.66$) and respectively of b^* the mean Nusselt number no longer increases.
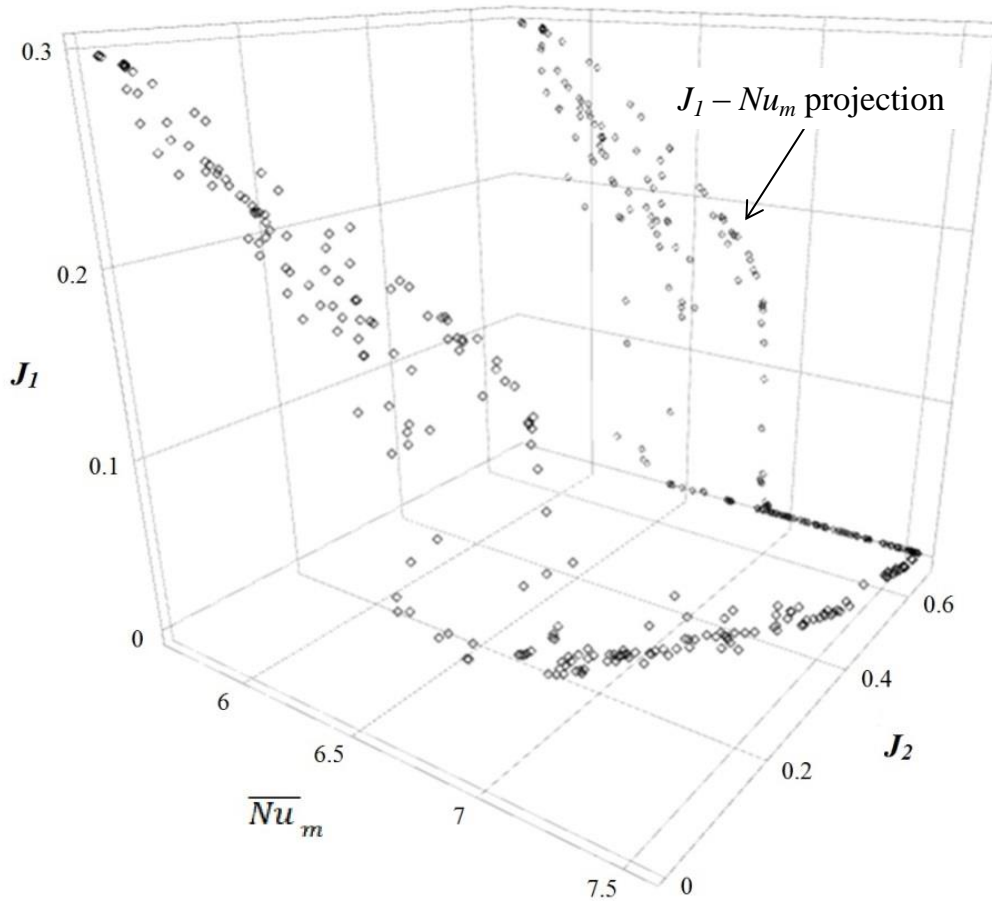
Fig. 18. *Re*=90: Solutions of the optimization problem in a three-dimensional space corresponding to the three objective functions J_1, J_2 and $\overline{Nu_m}$; the projection of the solutions at the level defined by objective function J_1 vs. mean Nusselt number, $\overline{Nu_m}$, is also included.
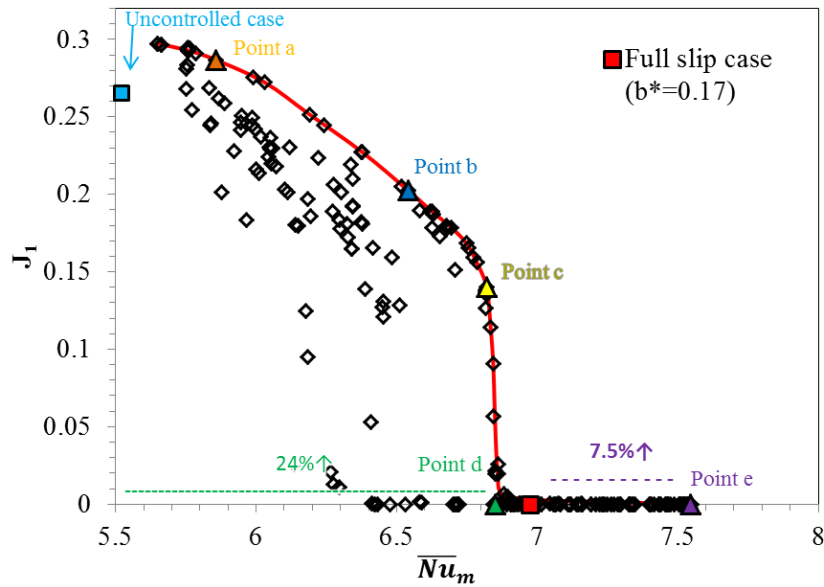
Fig. 19. *Re*=90: projection of the solutions at the level defined by objective function J_1 and the mean Nusselt number, $\overline{Nu_m}$, and sketch of the corresponding Pareto front. The uncontrolled case is included and five Pareto front solutions are highlighted. Point e corresponds to the stabilised case at a maximum mean Nusselt number.
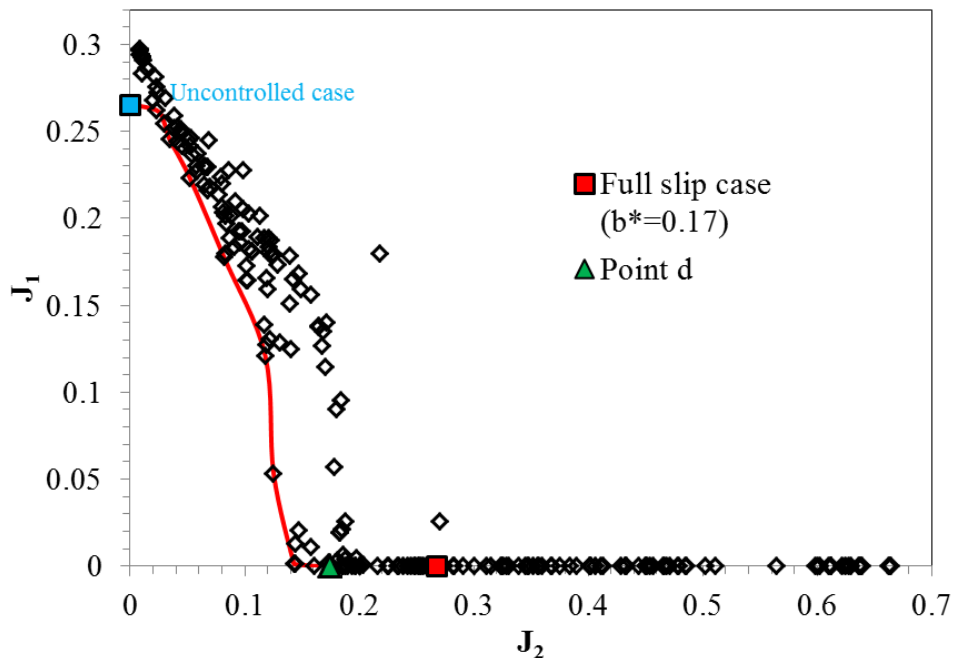
Fig. 20. *Re*=90: projection of the solutions at the level defined by objective function J_1 and objective function J_2, and sketch of the corresponding Pareto front. The uncontrolled case, as well as the stabilized solution at the minimum control effort (Point d), are highlighted.
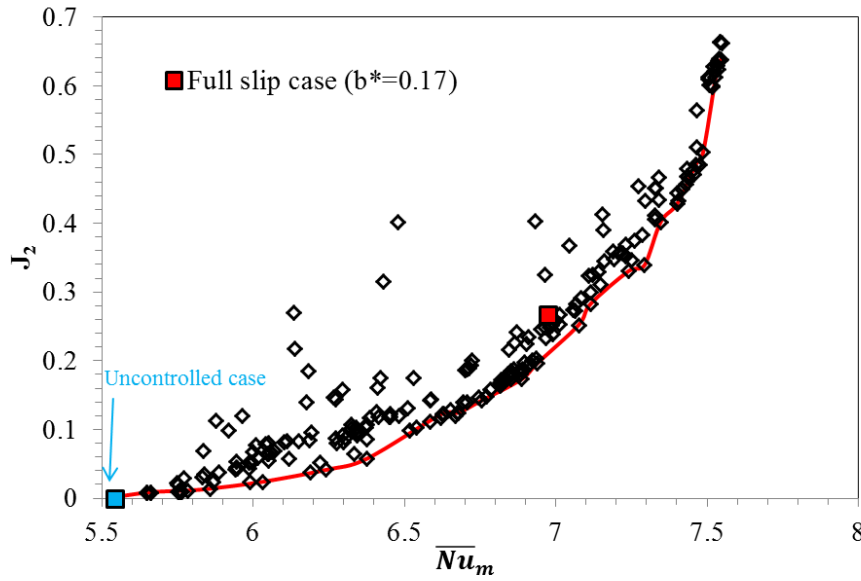
Fig. 21. *Re*=90: projection of the solutions at the level defined by objective function J_2, and the mean Nusselt number, $\overline{Nu_m}$, and sketch of the corresponding Pareto front. The uncontrolled case as, well as the full slip case, are highlighted.

In Fig. 19 five representative solutions of the Pareto front are depicted with colored triangles by Points a-e; the uncontrolled case and the full slip case for b^*=0.17 are also included. The corresponding design variables and objective function values are reported in Table 2.

Fig. 22 presents the calculated slip velocity distributions, as well as the vorticity isocontours. It is shown, that for three out of the five cases, namely Points b, c and e, the hydrophobic region includes the front stagnation point region, while for all the cases slip is disabled in the rear stagnation point region. Considering that those cases represent non-dominated cases regarding the time-averaged mean Nusselt number, the earlier indications (Section 3.2) are confirmed, showing that control effort can be substantially reduced at the same time achieving optimal solutions in terms of heat transfer enhancement. The vorticity isocontours demonstrate that cases a-c are unstable due to the formation of the Kármán vortex street, while cases d and e correspond to a stabilized flow.

On the other hand, Fig. 23 presents the local Nusselt number distribution and the temperature iso-contours for the solutions corresponding to solutions depicted by Points a-e in Fig. 19. Fig. 23 demonstrates, that for the solutions depicted by the Points b, c and e, the local Nusselt number distribution attains a smooth transition in the front stagnation point region, due to hydrophobicity. On the contrary, solutions depicted by Points a and d attain a more sharp transition of the local Nusselt distribution from the

front stagnation point region to the sideway regions of the cylinder. Here, it could be suggested that flow solutions depicted by Point a and Point d would benefit from the application of hydrophobicity in the front stagnation point region, in terms of heat transfer enhancement. In more detail Point d corresponds to an optimal solution in respect with the minimization of both the control effort and flow unsteadiness; in this case the vortex street is fully cancelled. However, it is already demonstrated, that the lack of hydrophobicity in the front stagnation point region hinders a further increase of the mean Nusselt number. Finally, the temperature isocontours (Fig. 23) demonstrate a similar structure to the one of the vorticity isocontours (Fig. 22).

Table 2. *Re*=90: design variable values and corresponding objective function values, for the uncontrolled case, as well as for cases a to e.

Case	b^*	θ_{min}	θ_{max}	$\varphi=\theta_{max}-\theta_{min}$	J_1	J_2	$\overline{\overline{Nu}}_m$
Uncontrolled	0.000	0.00°	0.00°	0.00°	0.308	0.000	5.520
Point a	0.016	12.20°	114.85°	102.65°	0.287	0.014	5.857
Point b	0.080	5.03°	153.26°	148.23°	0.203	0.103	6.540
Point c	0.130	0.00°	150.91°	150.91°	0.140	0.172	6.820
Point d	0.174	23.97°	138.57°	114.60°	0.000	0.174	6.850
Point e	0.442	5.24°	170.47°	165.23°	0.000	0.638	7.545
Full slip, stabilized flow	0.170	0.00°	180.00°	180.00°	0.000	0.267	6.974
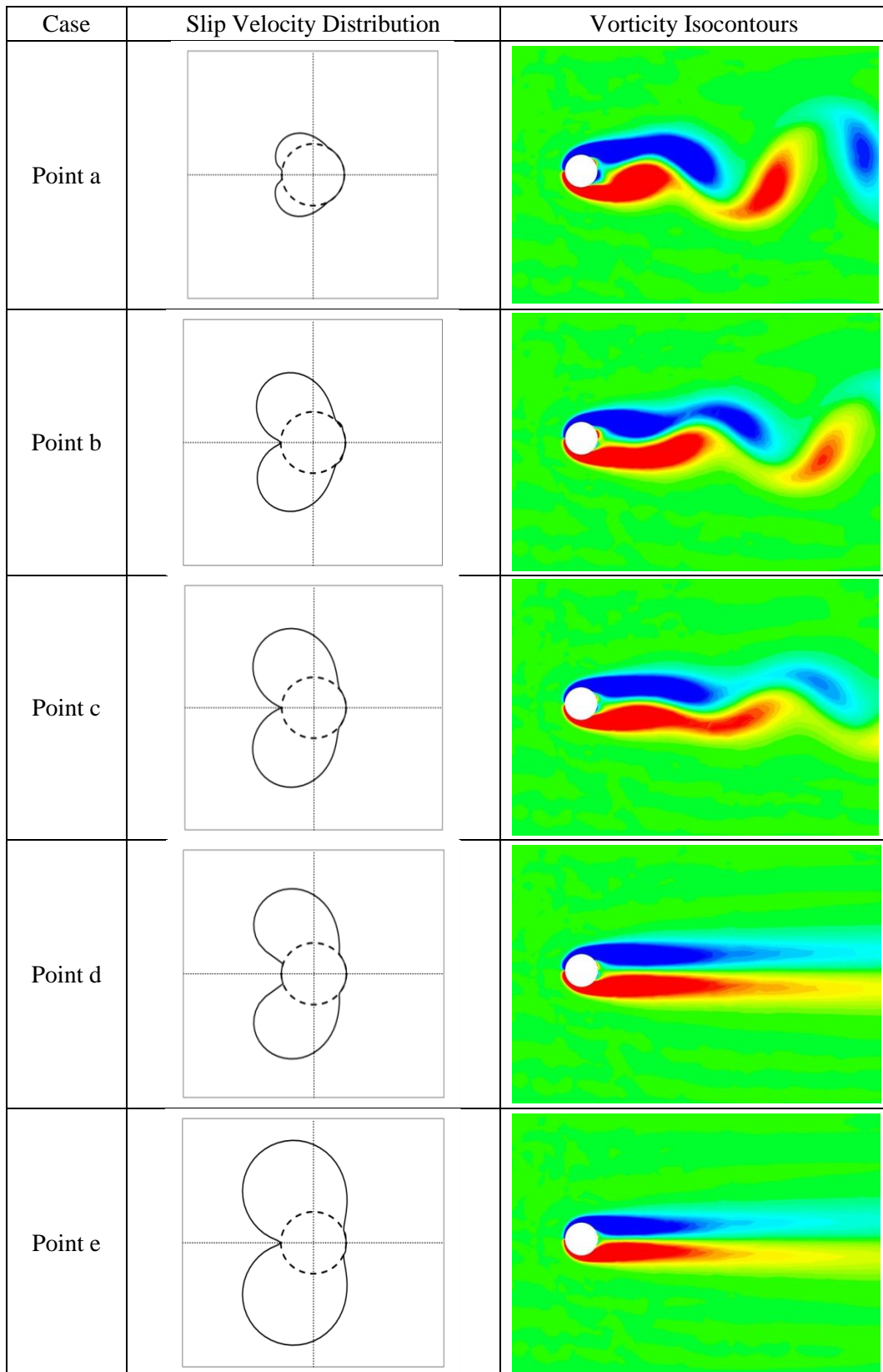
Fig. 22. *Re*=90: computed slip velocity profiles of base flow corresponding to solutions a to e (left column) and color-coded contours of instantaneous vorticity in the non-linear flow state (right column).

Case	Local Nusselt Distribution	Temperature Isocontours
Point a		
Point b		
Point c		
Point d		
Point e		

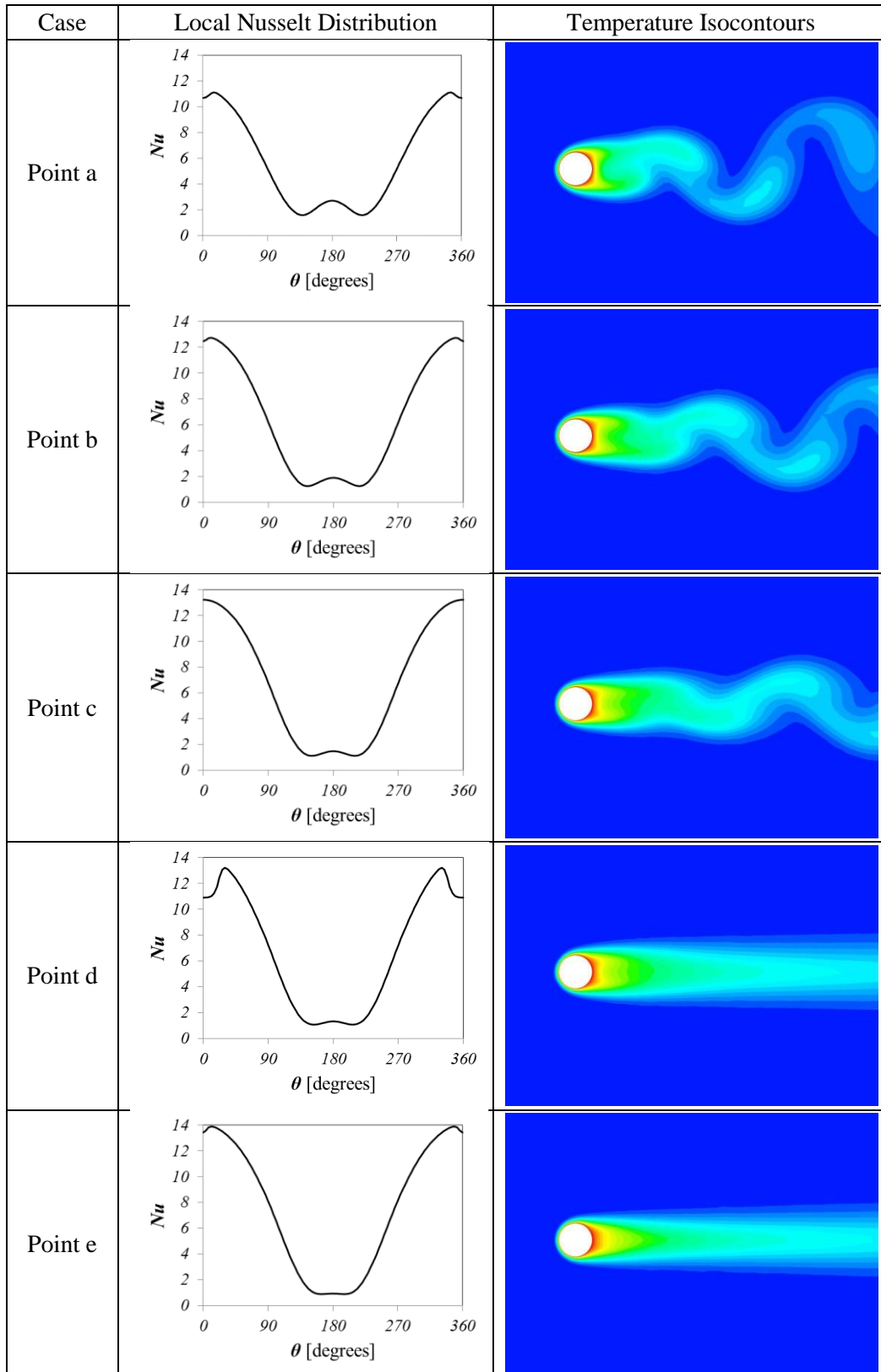**Fig. 23.** *Re*=90: local Nusselt number distribution along the cylinder surface corresponding to solutions a to e (left column) and color-coded contours of instantaneous temperature in the non-linear flow state (right column).

In order to demonstrate the adequacy of the search space extent, the variation of all three design variables along the Pareto front is presented in. Fig. 24 verifies a more pronounced increase in the first component of the control effort, $b*$, in comparison to the second one, φ, at increasing total control effort (J_2). In particular, regarding φ, its increase is due to the rapid increase in θ_{max}, while θ_{min} tends to zero. As a result, for the majority of the solutions lying on the Nu-J_1 projection of the Pareto front both the θ_{max} angle and the extent of hydrophobicity φ converge to about 150°. These results suggest that slip should be applied on the entire cylinder surface excluding a region $\pm30^o$ from the rear stagnation point.

Finally, Fig. 25 presents the results of a detailed sensitivity analysis around the optimal solution depicted by Point d in Fig. 19. Fig. 25i and Fig. 25ii present the values of the objective function J_1 and Nu respectively, as a function of the three design variables ($b*$, θ_{min}, θ_{max}); for each case two design variables are kept constant, while the third one is modified around the corresponding design variable value at Point d. The main goal here is to evaluate the accuracy of the optimization by investigating whether the solution (Point d) is actually optimal.

In Fig. 25a it is shown that a decrease in the slip length results in (i) unstable solutions (decrease in J_1), and (ii) a decrease of the mean Nusselt number. These results can be verified by the increase of the vorticity intensity and the decrease of the local Nusselt number, illustrated in Fig. 26. Further, a decrease in the extent of hydrophobicity, presented in Fig. 25b and Fig. 25c, results in (i) unstable solutions and (ii) lower mean Nusselt number.

On the other hand, by increasing the slip length (Fig. 25a) it is demonstrated that (i) the solutions remain stable (see Fig. 26) and (ii) the mean Nusselt number increases; the latter is in accordance with the results presented in Fig. 26. However, in these cases the control effort escalates, which is not acceptable. Finally, in Fig. 25b and Fig. 25c, an increase in the extent of hydrophobicity cause (i) destabilization of the flow, but results in (ii) higher Nusselt number values. As a result the optimal solution depicted by Point d is accurate in terms of control effort.

(a)

(b)

(c)

(d)
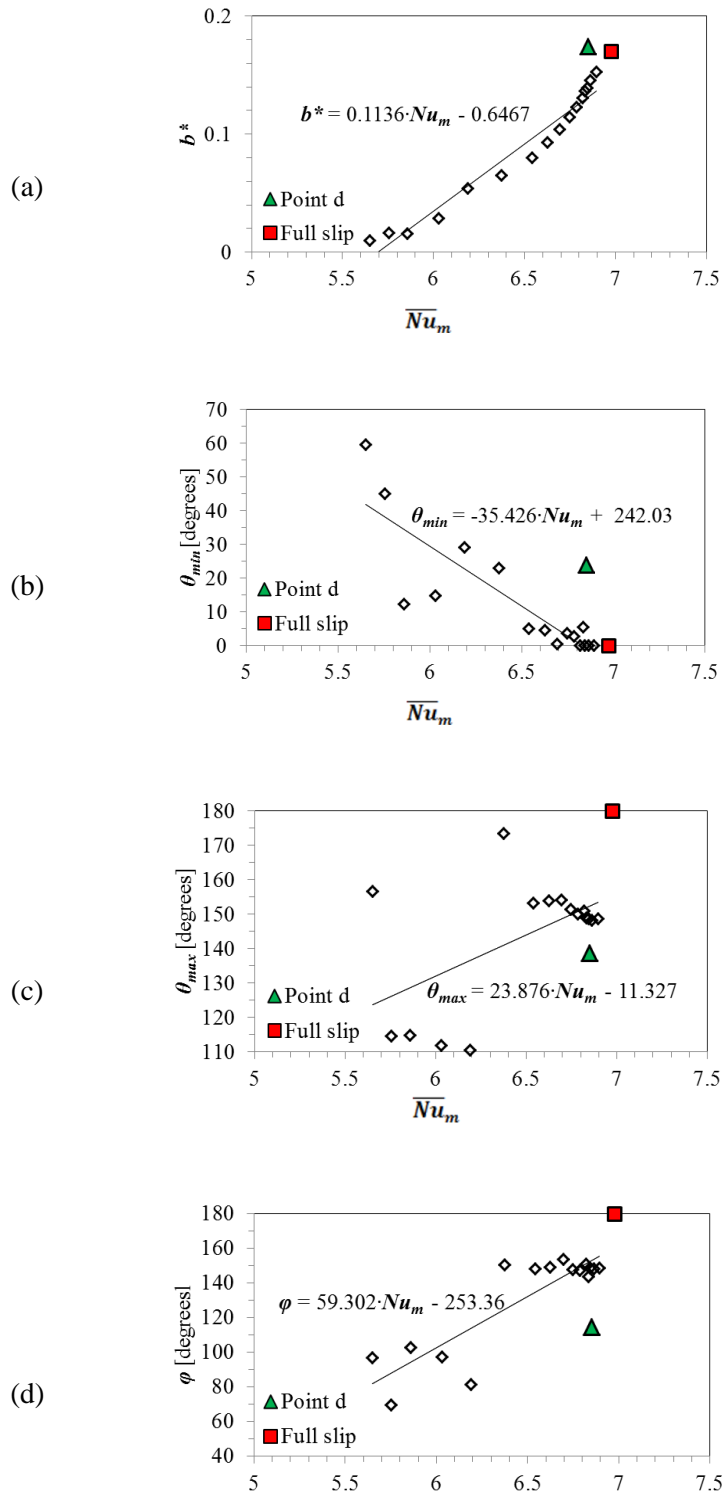
Fig. 24. *Re*=90: design variables versus the time-averaged mean Nusselt number for solutions lying on the projection of the Pareto front on the J_1-$\overline{Nu}_m$ plane. The case of stabilized flow with full slip is also included.
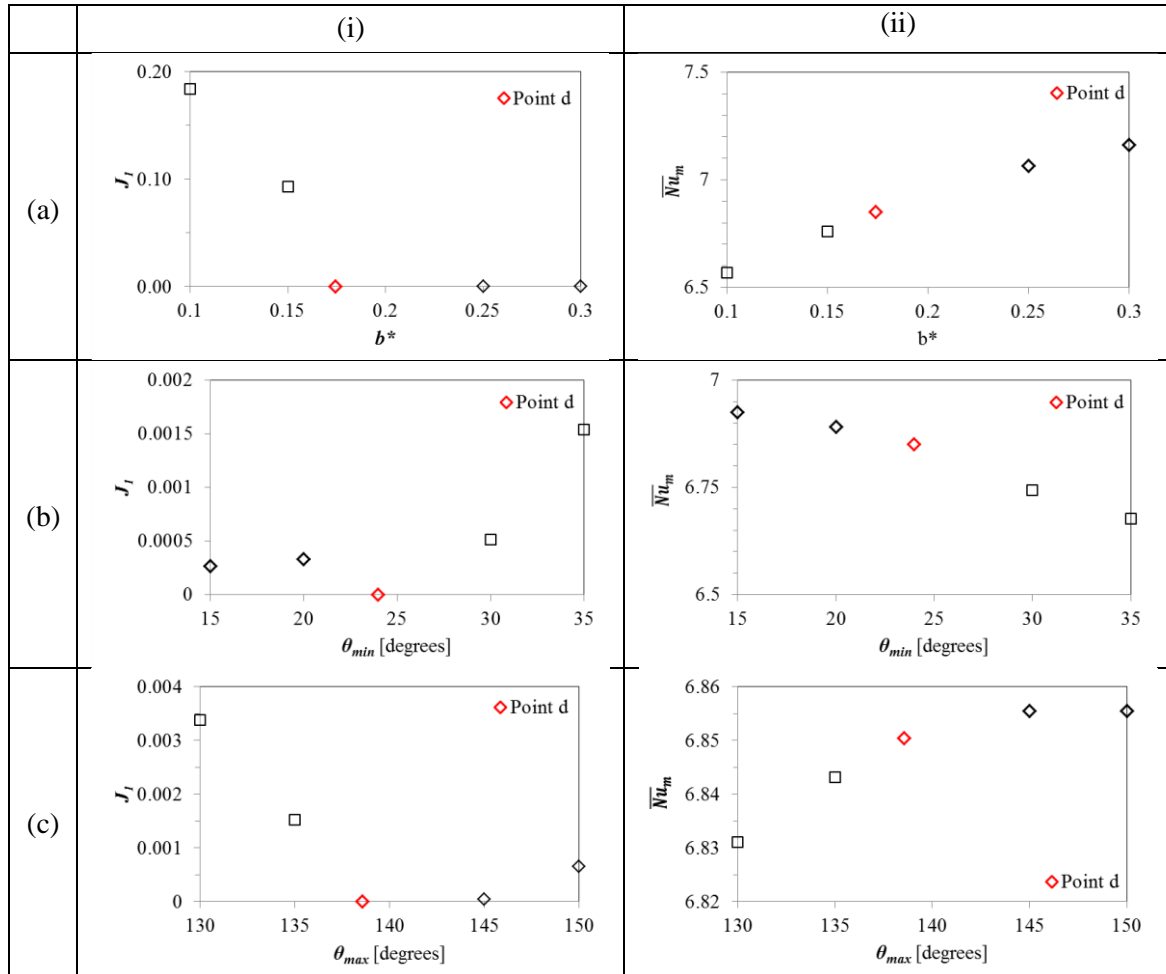
Fig. 25. Objective function J_1 and time-averaged mean Nusselt number, $\overline{Nu_m}$, versus the design variables (b^*, θ_{min}, θ_{max}). Each case correspond to one design variable fluctuating, namely (a) b^*, (b) θ_{min} and (c) θ_{max} while the remaining two as equivalent to those of Point d. The cases with control effort reduction in comparison with Point d are depicted with squares.

$b*$	(i) Vorticity Isocontours	(ii) Local Nusselt Distribution
0.1		
0.15		
0.174 (Point d)		
0.25		
0.3		
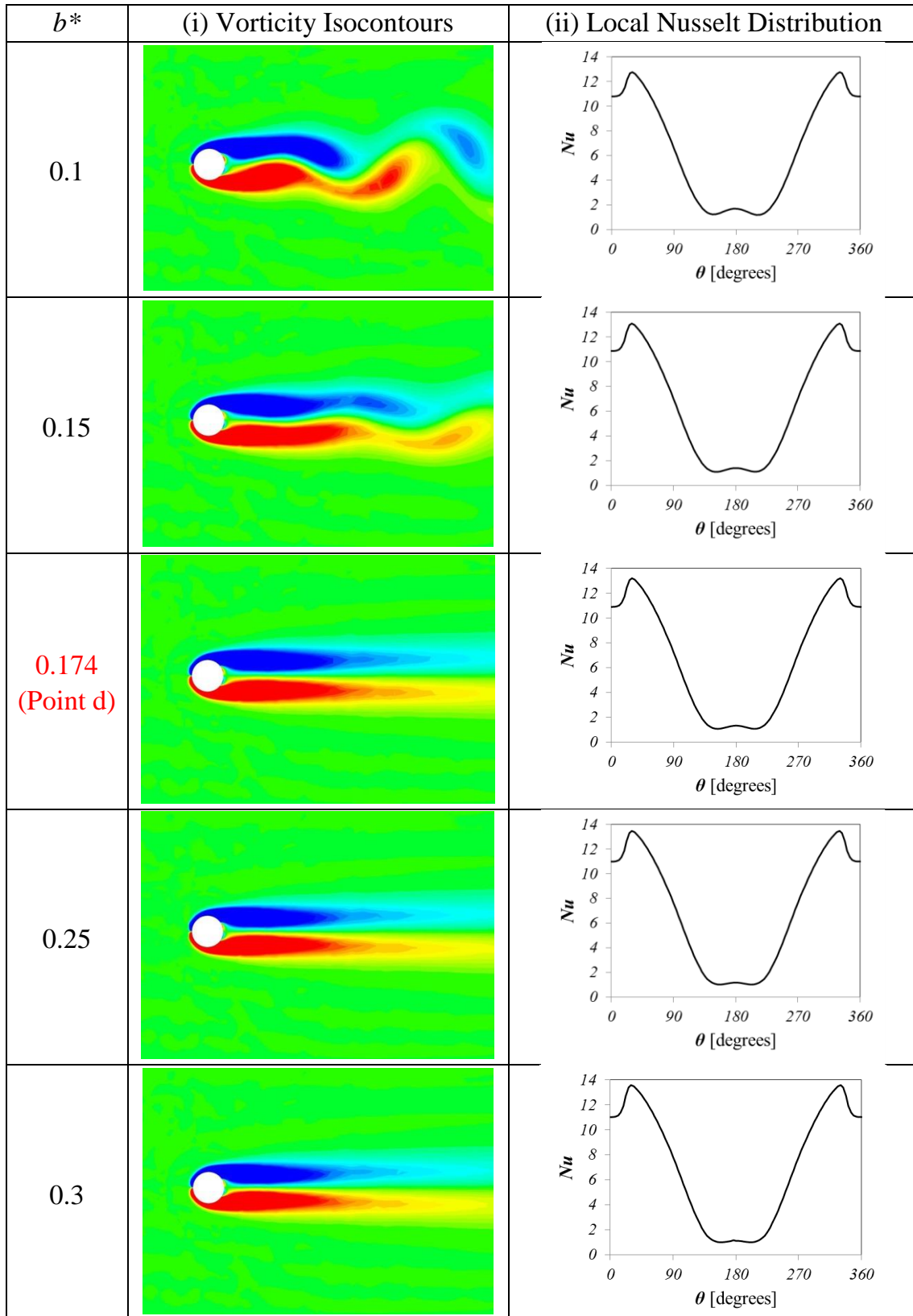
Fig. 26. *Re*=90: color-coded contours of instantaneous vorticity in the non-linear flow state (left column) and local Nusselt number distribution along the cylinder surface (right column), corresponding to solutions depicted in Fig. 25a.

43

4.5.2 Optimization results for Re=180

For *Re*=180, the optimization solutions are projected on the $\overline{Nu_m}$-J_1 and J_2-J_1 planes and are presented in Fig. 27 and Fig. 28 respectively. All three mappings demonstrate a similar structure to the one observed for *Re*=90 (see Fig. 19, Fig. 20).

Fig. 27 establishes, that optimal solutions lying on the $\overline{Nu_m}$-J_1 projection of the Pareto front are characterized by increased mean Nusselt number values, in comparison to the corresponding case, for *Re*=90 (Fig. 19). The latter is in accordance with the indicative observations for the full slip case, related to the heat transfer enhancement due to the Reynolds number increase (see Section *3.1.1*). Further, five representative solutions of the Pareto front (Points a-e), as well as the one corresponding to uncontrolled flow, and the stabilized full slip case at a minimal slip length (*b**=0.25) are depicted in Fig. 27. In order to investigate in more detail the solutions depicted in Fig. 27, the corresponding vorticity isocontours and the local Nusselt number distributions are presented in Fig. 29. Fig. 29 shows, that as the control effort increases, the vorticity intensity is reduced; the solution depicted in Fig. 27 by Point e corresponds to vortex street cancelation at the maximal Nusselt number. On the other hand, the distribution of the local Nusselt number exhibits a similar behavior to the *Re*=90 case. Here, an increase in the control effort results in smooth local Nusselt number distributions in the rear stagnation point region.

Finally, Fig. 28 presents the projection of the Pareto front on the J_2-J_1 plane. Here, Point f depicts the optimal solution corresponding to the vortex street cancelation at the minimal control effort, for *Re*=180. The corresponding vorticity isocontours demonstrate the global flow stabilization, whereas the local Nusselt number distribution reflects the enhancement in comparison with the uncontrolled case (Fig. 30).

The values of design variables and objective functions of all the cases are reported in Table 3. Table 3 demonstrates that a maximum of 38% enhancement, regarding heat transfer, is achieved for Point e, in comparison with the uncontrolled case. The solution depicted by Point f in Fig. 28 is characterized by a reduction of control effort of 12% in comparison with the full slip case.
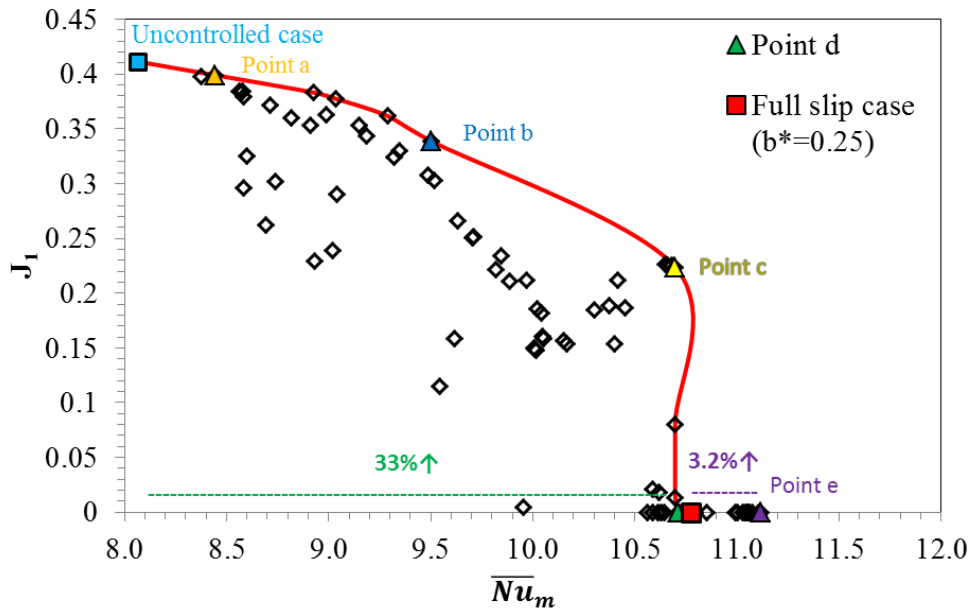
Fig. 27. : *Re*=180: projection of the solutions at the level defined by objective function J_1 and the mean Nusselt number, $\overline{Nu_m}$, and sketch of the corresponding Pareto front. The uncontrolled case is included and five non-dominated cases are highlighted. In specific, Point e is the stable case with maximum mean Nusselt number.
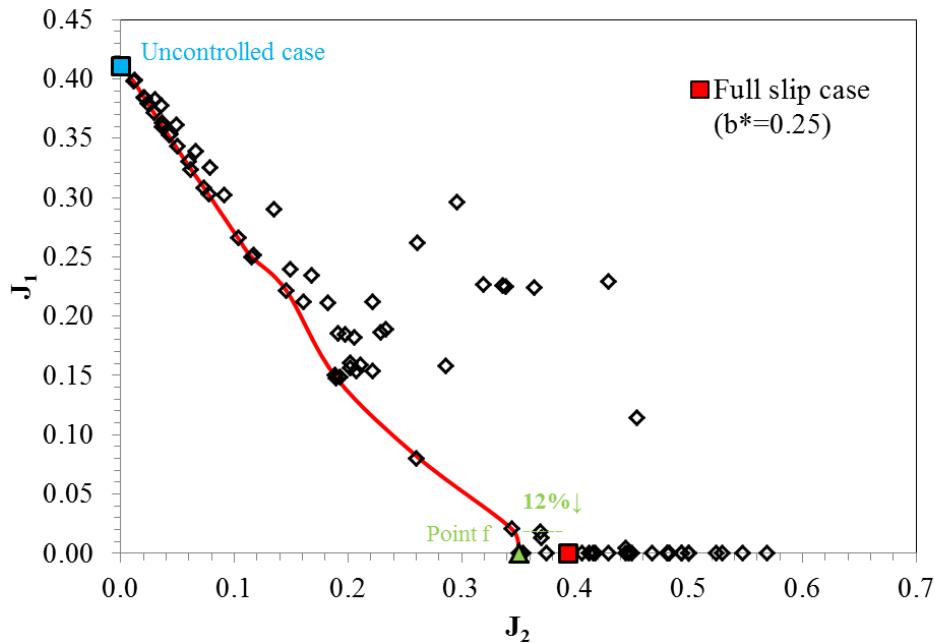
Fig. 28. *Re*=180: projection of the solutions at the level defined by objective function J_1 and the objective function J_2, and sketch of the corresponding Pareto front. The uncontrolled case, as well as the stable case at the minimum control effort (Point f) are highlighted.
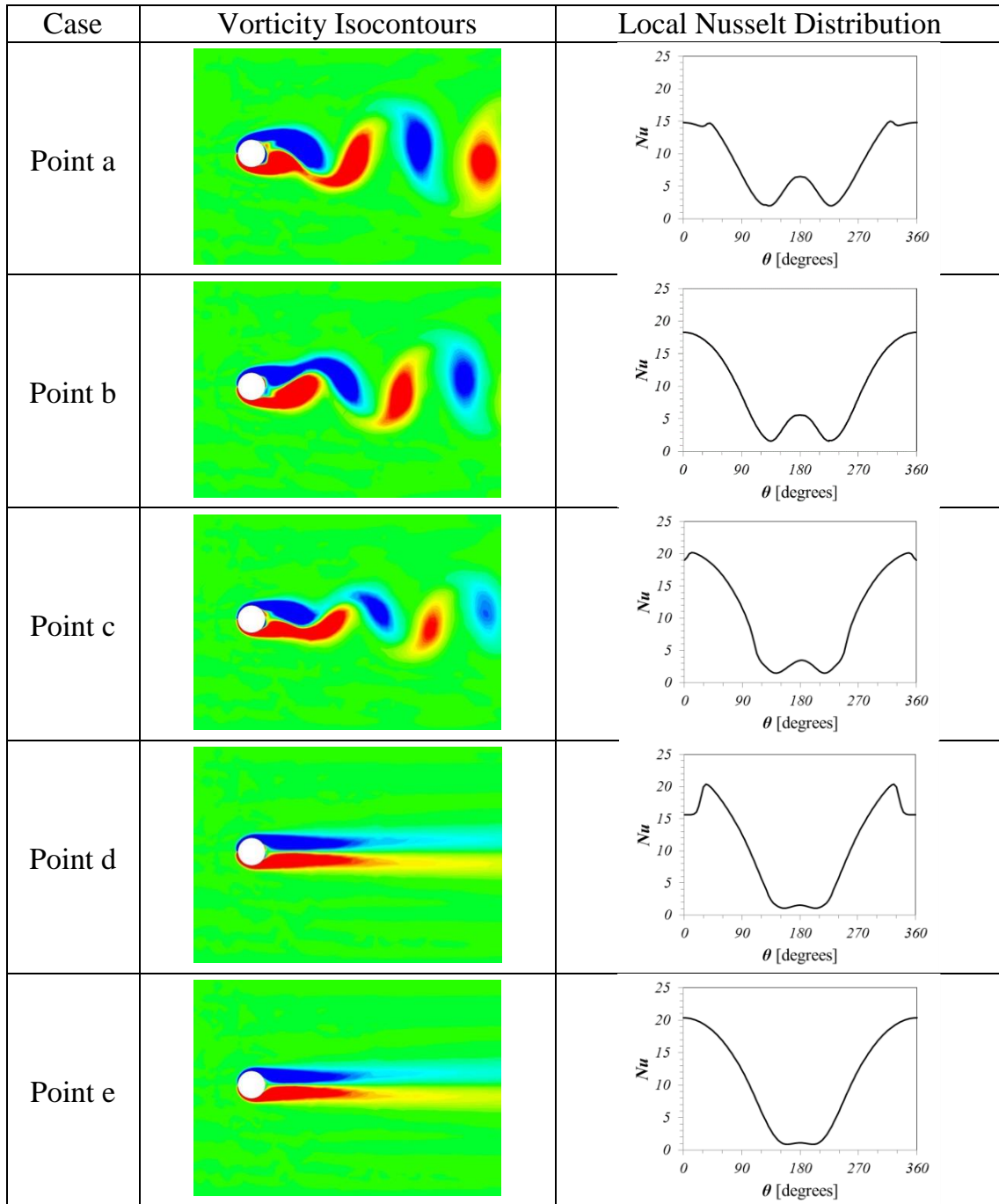
Case	Vorticity Isocontours	Local Nusselt Distribution
Point a		
Point b		
Point c		
Point d		
Point e		

Fig. 29. *Re*=90: color-coded contours of instantaneous vorticity in the non-linear flow state (left column) and local Nusselt number distribution along the cylinder surface (right column), corresponding to solutions depicted in Fig. 27

46

Case	Vorticity Isocontours	Local Nusselt Distribution
Point f		
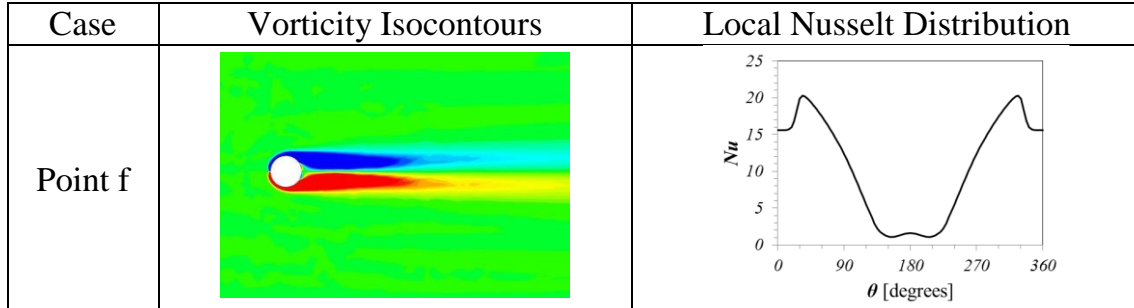
Fig. 30. *Re*=90: color-coded contours of instantaneous vorticity in the non-linear flow state (left column) and local Nusselt number distribution along the cylinder surface (right column), corresponding to solution depicted in Fig. 28.

Table 3. *Re*=180: design variable values and corresponding objective function values, for the uncontrolled case, as well as for cases a to f.

| Case	b^*	θ_{min}	θ_{max}	$\varphi=\theta_{max}-\theta_{min}$	J_1	J_2	$\overline{Nu}_m$
Uncontrolled	0.000	0.00°	0.00°	0.00°	0.411	0.000	8.064
Point a	0.010	35.78°	177.66°	141.88°	0.399	0.012	8.445
Point b	0.043	0.003°	176.44°	176.44°	0.339	0.066	9.500
Point c	0.383	5.44°	114.10°	108.66°	0.224	0.364	10.697
Point d	0.430	26.04°	135.79°	109.75°	0.000	0.412	10.710
Point e	0.378	1.85°	167.63°	165.78°	0.000	0.547	11.118
Point f	0.369	26.89°	135.76°	108.87°	0.000	0.350	10.630
Full slip, stabilized flow	0.250	0.00°	180.00°	180.00°	0.000	0.393	10.775

5. CONCLUSIONS

The present computational work has investigated the problem of heat transfer in a flow past a circular cylinder at low Reynolds numbers, by means of a passive control scheme utilizing surface hydrophobicity.

Firstly, slip conditions were applied on the entire cylinder surface. It was demonstrated, that the increase in the slip length leads simultaneously to suppression of the flow unsteadiness and to a substantial heat transfer enhancement. However, it was noticed, that application of hydrophobicity in the rear stagnation point region induces destabilizing effects and imposes a local negative effect regarding heat transfer; the local Nusselt number is there reduced.

Next, in order to avoid these negative effects, as well as to decrease the extent of the hydrophobic region and the associated cost, hydrophobicity is not applied in the rear stagnation point region. The results demonstrated, that application of hydrophobicity on the remaining part of the cylinder results in the same enhancement levels of heat transfer, as in the full slip case and in stronger stabilizing effects.

Finally, guided by the initial simulations and results, a multi - objective optimization problem was formulated aiming at the identification of optimal combinations of the slip length and the extent of the hydrophobic region. This optimization problem addressed three goals, namely: (a) the heat transfer enhancement, (b) the flow stabilization and (c) the reduction of the associated cost, in terms of the slip length of the hydrophobic material and the extent of the hydrophobic region. All these goals were quantified by the introduction of proper objective functions. The optimization problem was solved, by means of genetic algorithms, for two representative Reynolds number values.

The present results have demonstrated that optimal application of partial slip is more effective than full slip in suppressing flow unsteadiness. At the same time, in the partial slip setup the heat transfer attains the same enhancement levels as in the full slip case. It should be noted, that in both the full and the partial slip cases, an increase up to 37% in the mean Nusselt number in comparison with the uncontrolled cases, is demonstrated. On the other hand optimal application of partial slip can result in a decrease of control effort by up to 35%, leading thus to a substantial decrease of the associated cost.

REFERENCES

1. Nakamura H., Igarashi T. Variation of Nusselt number with flow regimes behind a circular cylinder for Reynolds numbers from 70 to 30000. Int. J. Heat Mass Transfer 2004;47:5169-5173.

2. Sanitjai S., Goldstein R. Forced convection heat transfer from a circular cylinder in crossflow to air and liquids. Int. J. Heat Mass Transfer 2004;47:4795-4805.

3. Bharti R., Chhabra R.P., Eswaran V. Steady forced convection heat transfer from a heated circular cylinder to power-law fluids. Int. J. Heat Mass Transfer 2007;50:977-990.

4. Vegad M., Satadia S., Pradip P., Chirag P., Bhargav P. Heat Transfer Characteristics of Low Reynolds Number Flow of Nanofluid Around a Heated Circular Cylinder. Procedia Technology 2014;14:348-356.

5. Patnana V., Bharti R., Chhabra R. Two-dimensional unsteady forced convection heat transfer in power-law fluids from a cylinder. Int. J. Heat Mass Transfer 2010;53:4152-4167.

6. Baranyi L. Computation of unsteady momentum and heat transfer from a fixed circular cylinder in laminar flow. Journal of Computational and Applied Mechanics 2003;4.1:13-25.

7. Golani R., Dhiman A.K. Fluid flow and heat transfer across a circular cylinder in the unsteady flow regime. IJES 2014;3.3:8-19.

8. Harimi I., Saghafian M. Numerical simulation of fluid flow and forced convection heat transfer from tandem circular cylinders using overset grid method. J. Heat Transf. 2011;28:309-327.

9. Karniadakis G. Numerical simulation of forced convection heat transfer from a cylinder in crossflow. Int. J. Heat Mass Transfer 1987;31:107-118.

10. Pourgholam M., Izadpanah E., Motamedi R., Habibi S.E. Convective heat transfer enhancement in a parallel plate channel by means of rotating or oscillating blade in the angular direction. Applied Thermal Engineering 2015;78:248-257.

11. Bovand M., Rashidi S., Esfahani J. Enhancement of heat transfer by nanofluids and orientations of the equilateral triangular obstacle. Energy Conversion and Management 2015;97:212-223.

12. Ziyad K., Saleh M., Ali Y. Heat transfer enhancement in combined convection around a horizontal cylinder using nanofluids. J. Heat Transf. 2008;130(8).

13. Haase S., Chapman J., Tsai P., Lohse D., Lammertink G. The Graetz_Nusselt problem extended to continuum flows with finite slip. J. Fluid Mech. 2015;764:R3.

14. Maynes D, Webb BW, Davies J. 2008. Thermal transport in a microchannel exhibiting ultrahydrophobic microribs maintained at constant temperature. J. Heat Transf. 130:022402

15. Rothstein JP. Slip on superhydrophobic surfaces. Ann Rev Fluid Mech 2010;41:89-109.

16. Roshko A. On the wake and drag of bluff bodies. J Aerosp Sci 1955;22:124-132.

17. Strykowski PJ, Sreenivasan KR. On the formation and suppression of vortex 'shedding' at low Reynolds numbers. J Fluid Mech 1990;218:71-107.

18. Mittal S, Raghuvanshi A. Control of vortex shedding behind circular cylinder for flows at low Reynolds numbers. Int J Num Meth Fluids 2001;35(4): 421–447.

19. Yildirim I, Rindt CCM, Steenhoven AA (2010). Vortex dynamics in a wire-disturbed cylinder wake. Phys Fluids 2010;22 (9): 094101.

20. Muralidhar P, Ferrer N, Daniello R, and Rothstein JP. Influence of Slip on the Flow Past Superhydrophobic Circular Cylinders. J Fluid Mech 2011;680:459–476.

21. You D, Moin P. Effects of Hydrophobic Surfaces on the Drag and Lift of a Circular Cylinder. Phys Fluids 2007;31(8):08170.

22. Mastrokalos M., Papadopoulos C., Kaiktsis L. Optimal stabilization of a flow past a partially hydrophobic circular cylinder. Comp. & Fluids 2015;107:256-271.

23. Delaunay Y, Kaiktsis L. Control of circular cylinder wakes using base mass transpiration. Phys Fluids 2001;13:3285–3302.

24. Wood CJ. Visualization of an incompressible wake with base bleed. J Fluid Mech 1967;29:259–272.

25. Dong S, Triantafyllou GS, Karniadakis GE (2008). Elimination of vortex streets in bluff-body flows. Phys Rev Lett 2008; 100(20):204501.

26. Tokumaru PT, Dimotakis PE. Rotary oscillation control of a cylinder wake. J Fluid Mech 1991;224:77–90.

27. Tokumaru PT, Dimotakis PE. The lift of a cylinder executing rotary motions in a uniform flow. J Fluid Mech 1993;255:1-10.

28. Mittal S, Kumar B. Flow past a rotating cylinder. J Fluid Mech 2003;476: 303–34.

29. Lecordier JC, Hamma L, and Paranthoen P. The control of vortex shedding behind heated circular cylinders at low Reynolds numbers. Exp Fluids 1991;10:224–229.

30. Chen Z, Aubry N. Active control of cylinder wake. Communications in Nonlinear Science and Numerical Simulation 2003;10:205–216.

31. Legendre D, Lauga E, Magnaudet J. Influence of slip on the dynamics of two-dimensional wakes. J Fluid Mech. 2009;633:437–447.

32. Seo IW, Song CG. Numerical simulation of laminar flow past a circular cylinder with slip conditions. Int. J. Numer. Meth. Fluids 2012;68:1538–1560.

33. Zhang, WM, Meng G, Wei X. A review on slip models for gas microflows. Microfluidics and Nanofluidics 2012; 13(6):845–882.

34. Kaiktsis L, Triantafyllou GS, Özbas M. Excitation, inertia, and drag forces on a cylinder vibrating transversely to a steady flow. J Fluids and Structures 2007;23:1–21.

35. Evangelinos C, Karniadakis GE. Dynamics and flow structures in the turbulent wake of rigid and flexible cylinders subject to vortex-induced vibrations. J Fluid Mech. 1999;400:91–124.

36. Dhiman A., Ghosh R. Computer simulation of momentum and heat transfer across an expanded trapezoidal bluff body. J. Heat Transf. 2013;59:338-352.

37. Fonseca CM, Fleming PJ. An overview of evolutionary algorithms in multiobjective optimization. Evol. Comput. 1995;3:1–16.

38. Cahon S, Melab N, Talbi EG. ParadisEO: A framework for the reusable design of parallel and distributed metaheuristics. J. Heuristics 2004;10:357–380.

39. Deb K, Pratap A, Agarwal S, Meyarivan T. A fast and elitist multiobjective genetic algorithm: NSGA-II. IEEE Transactions on Evolutionary Computation 2002;6:182-197.